

Direct Observation and Analysis of Low-Energy Magnons with Raman Spectroscopy in Atomically Thin NiPS₃

*Woongki Na,^{†, #} Pyeongjae Park,^{‡, §, #} Siwon Oh,^{†, #} Junghyun Kim,[‡] Allen Scheie,[⊥] David Alan
Tennant,[¶] Hyun Cheol Lee,^{†, *} Je-Geun Park,^{‡, *} Hyeonsik Cheong,^{†, *}*

[†]Department of Physics, Sogang University, Seoul 04107, Korea

[‡]Department of Physics and Astronomy, Seoul National University, Seoul 08826, Korea

[§]Materials Science and Technology Division, Oak Ridge National Laboratory, Oak Ridge,
Tennessee 37831, USA

[⊥]MPA-Q, Los Alamos National Laboratory, Los Alamos, NM 87545, USA

[¶]Department of Physics and Astronomy, University of Tennessee, Knoxville, TN 37996, USA
and Department of Materials Science and Engineering, University of Tennessee, Knoxville, TN
37996, USA

[#]These authors contributed equally: Woongki Na, Pyeongjae Park, Siwon Oh

ABSTRACT

Van der Waals (vdW) magnets have rapidly emerged as a fertile playground for novel fundamental physics and exciting applications. Despite the impressive developments over the past few years, technical limitations pose a severe challenge to many other potential breakthroughs. High on the list is the lack of suitable experimental tools for studying spin dynamics on atomically thin samples. Here, Raman scattering techniques are employed to observe directly the low-lying magnon (~ 1 meV) even in bilayer NiPS₃. The unique advantage is that it offers excellent energy resolutions far better on low-energy sides than most inelastic neutron spectrometers can offer. More importantly, with appropriate theoretical analysis, the polarization dependence of the Raman scattering by those low-lying magnons also provides otherwise hidden information on the dominant spin-exchange scattering paths for different magnons. By comparing with high-resolution inelastic neutron scattering data, these low-energy Raman modes are confirmed to be indeed of magnon origin. Because of the different scattering mechanisms involved in inelastic neutron and Raman scattering, this new information is fundamental in pinning down the final spin Hamiltonian. This work demonstrates the capability of Raman spectroscopy to probe the genuine two-dimensional spin dynamics in atomically-thin vdW magnets, which can provide novel insights that are obscured in bulk spin dynamics.

Notice: This manuscript has been authored by UT-Battelle, LLC, under contract DE-AC05-00OR22725 with the US Department of Energy (DOE). The US government retains and the publisher, by accepting the article for publication, acknowledges that the US government retains a nonexclusive, paid-up, irrevocable, worldwide license to publish or reproduce the published form of this manuscript, or allow others to do so, for US government purposes. DOE will provide public access to these results of federally sponsored research in accordance with the DOE Public Access Plan (<https://www.energy.gov/doe-public-access-plan>).

INTRODUCTION

Two-dimensional (2D) magnetism occupies a special place in modern condensed matter physics. A complete theoretical understanding of the three fundamental Hamiltonian models—Ising, XY, and Heisenberg—has provided profound insights into a variety of magnetic phenomena and beyond.¹⁻⁴ Despite the impressive breakthroughs in the theory, progress has been much slower on the experimental side, although numerous attempts have been made from the 1960s to 1980s.⁵⁻⁷ This was primarily due to the lack of suitable materials that realize the 2D magnetism, namely atomically thin sheets of magnetic materials. This gap motivated the initial exploration and eventual discovery of what are now known as van der Waals (vdW) magnets⁸. Notably, several demonstrations of monolayer magnetism have since been made in both antiferromagnetic and ferromagnetic systems within the Ising class, marking important experimental milestones.⁹⁻¹¹

During the past few years, several investigations on this newly discovered category of materials have demonstrated properties distinct from three-dimensional magnetic systems,¹² reinforcing the belief that vdW magnets could usher in a new era of 2D magnetism. However, further experimental advancements are required to fully probe their unique two-dimensional characteristics undisclosed in the bulk phase. High on the wish list is the experimental technique that can measure the spin dynamics of atomically thin vdW magnets. Notably, spin dynamics provide valuable information about the spin Hamiltonian, a must for any magnetic materials. Historically, inelastic neutron scattering (INS) has played a crucial role in elucidating the spin dynamics of bulk 3D materials, greatly advancing our understanding of the spin models for bulk magnetism since the late 1950s.¹³⁻¹⁶ However, an alternative technique is needed for atomically thin vdW samples due to a very small INS cross-section.¹⁷

Among several vdW magnets, NiPS₃ has recently gained significant interest, exhibiting XXZ-type antiferromagnetic ordering below the Néel temperature (T_N) of 155 K.^{18, 19} Its T_N decreases slightly as the number of layers is reduced from bulk to two layers but is suppressed in monolayers.¹⁹ Remarkably, this material exhibits extremely sharp many-body magnetic excitons, as observed in photoluminescence (PL) and absorption measurements.^{20, 21} Notably, these excitons are deeply connected to the local magnetic anisotropy of Ni sites,²² which can be studied by investigating the low-energy spin dynamics of NiPS₃.

Optical measurements can open a new opportunity to study the spin dynamics of NiPS₃ samples, from bulk to few layers. Although two recent INS studies have provided an overall understanding of the spin dynamics in NiPS₃,^{23, 24} its low-energy spin dynamics remain not fully understood. The primary challenge arises from the unclear low-energy INS profile due to pronounced instrumental resolution effects for NiPS₃.²⁴ This stems from a substantial mismatch of energy scales between the one-magnon bandwidth (55 meV) and low-energy excitations of interest (from 1 meV to 5 meV), resulting in a spectrum characterized by an excessively steep magnon dispersion which can be heavily impacted by the momentum resolution.²⁴ Instead, optical tools have provided clearer observations of the low-energy excitations.²⁵⁻²⁷ For example, the temperature-dependent THz emission measurements observed a sharp peak below the Néel temperature that redshifts from ~ 5 meV at 20 K, which weakens as the temperature increases towards T_N .²⁵ On the other hand, the pump-probe polarization rotation measurements observed two low-energy excitations at 0.3 THz (~ 1.2 meV) and 0.9 THz (~ 3.7 meV) at 10 K.²⁶ In addition, high-magnetic field (≥ 7 T) electron spin resonance (ESR) measurements yielded a resonance signal at 350 GHz (1.4 meV) at 4 K and 7 T.²⁷ The different energy values for these reports urgently call for more accurate and reliable measurements. Moreover, since all the measurements have been

conducted on bulk samples, the evolution of these low-energy magnon resonances in the atomically-thin limit, which can potentially reveal new aspects of the spin dynamics obscured in previous bulk studies, remains unanswered. For bulk magnetic materials, Raman scattering spectroscopy has been widely used to study the one- and two-magnon scattering processes, for which the work by Fleury and Loudon²⁸ has provided the classic principle for theoretical analysis. However, there has not yet been similar analysis on 2D magnetic systems experimentally or theoretically.

Here, we report on ultralow-frequency polarized Raman scattering measurements on atomically thin NiPS₃ down to monolayers. For bulk NiPS₃, three low-frequency modes are observed below T_N at 11, 31, and 40 cm⁻¹ at 3.8 K, labelled M₁, M₂, and M₃, respectively. The three modes have different dependences on polarization and temperature. M₁ is relatively stronger, and so we used it to study its dependence on the thickness. By comparing with the neutron scattering data, we can confirm the origin of M₁ and M₃ as being due to the magnon excitations. On the other hand, the polarization behaviors of these modes cannot be explained based on the classic theory by Fleury and Loudon,²⁸ for which we developed a more general theoretical model.

RESULTS

Raman Spectroscopy on Bulk NiPS₃. Figure 1 shows the crystal structure of NiPS₃. Monolayer NiPS₃ has a hexagonal structure, with the Ni atoms arranged in a hexagonal lattice. For the bulk, the layers are stacked with a slight shift along the *a*-axis (zigzag direction), forming a monoclinic structure. The Ni atoms are arranged in a hexagonal lattice, each surrounded by six S atoms with a trigonal antiprismatic arrangement. The layers are held together by weak van der Waals

interaction, allowing easy exfoliation. Below T_N , the spins are aligned in the ab plane, mainly along the a -axis, with the same-spin chains along the zigzag direction.²⁹

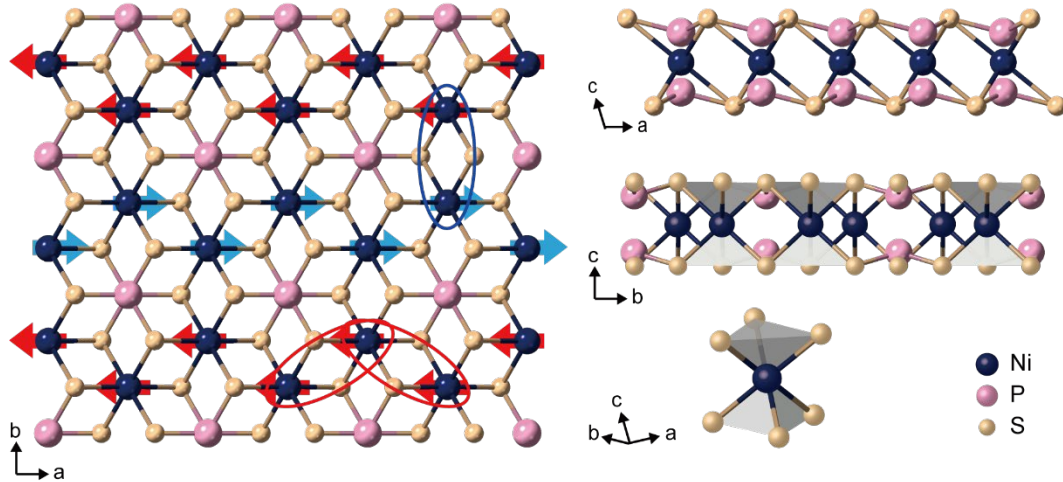


Figure 1. Crystal structure of NiPS₃. The large arrows indicate the spin directions showing the antiferromagnetic ordering. The blue and red ellipses indicate two possible types of spin pairs for the spin exchange scattering processes used in our theoretical calculations.

Figure 2a shows the temperature dependence of the polarized Raman spectra of a ~ 170 -nm-thick bulk NiPS₃ sample measured in $z(xx)\bar{z}$ and $z(xy)\bar{z}$ configurations, where z and \bar{z} indicate the directions of incident and scattered photons, respectively, and the variables inside the parenthesis indicate the polarization directions of the incident and scattered photons. Here, we set the x -direction 45° relative to the a -axis of the crystal determined by the polarization dependence of the photoluminescence at ~ 1.48 eV with those of the split Raman peaks at ~ 180 cm⁻¹ (Figure S1),²⁰ the splitting of which (ΔP_2) is a leading indicator of the antiferromagnetic ordering.¹⁹ At 290 K, the low-frequency Raman spectrum for the parallel [$z(xx)\bar{z}$] polarization configuration is dominated by the quasi-elastic scattering (QES) signal due to spin fluctuations, which is

suppressed at low temperatures.¹⁹ As the temperature is lowered below T_N of ~ 155 K, a sharp peak (M_1) and two weaker peaks (M_2 and M_3) emerge. These peaks become stronger and blueshift as the temperature is further lowered. Although M_1 overlaps with the QES signal, it can be resolved for temperatures of ~ 140 K and below. At 3.8 K, M_1 is at 11 cm^{-1} , corresponding to 0.33 THz or 1.4 meV, M_2 at 31 cm^{-1} (0.93 THz or 3.8 meV), and M_3 at 42 cm^{-1} (1.3 THz or 5.2 meV). The frequency of M_1 is also close to what was observed in the pump-probe polarization rotation measurements²⁶ or the ESR measurements,²⁷ and M_2 was also observed in the pump-probe measurements.²⁶ At the same time, M_3 is similar to that observed in the THz emission experiments.²⁵

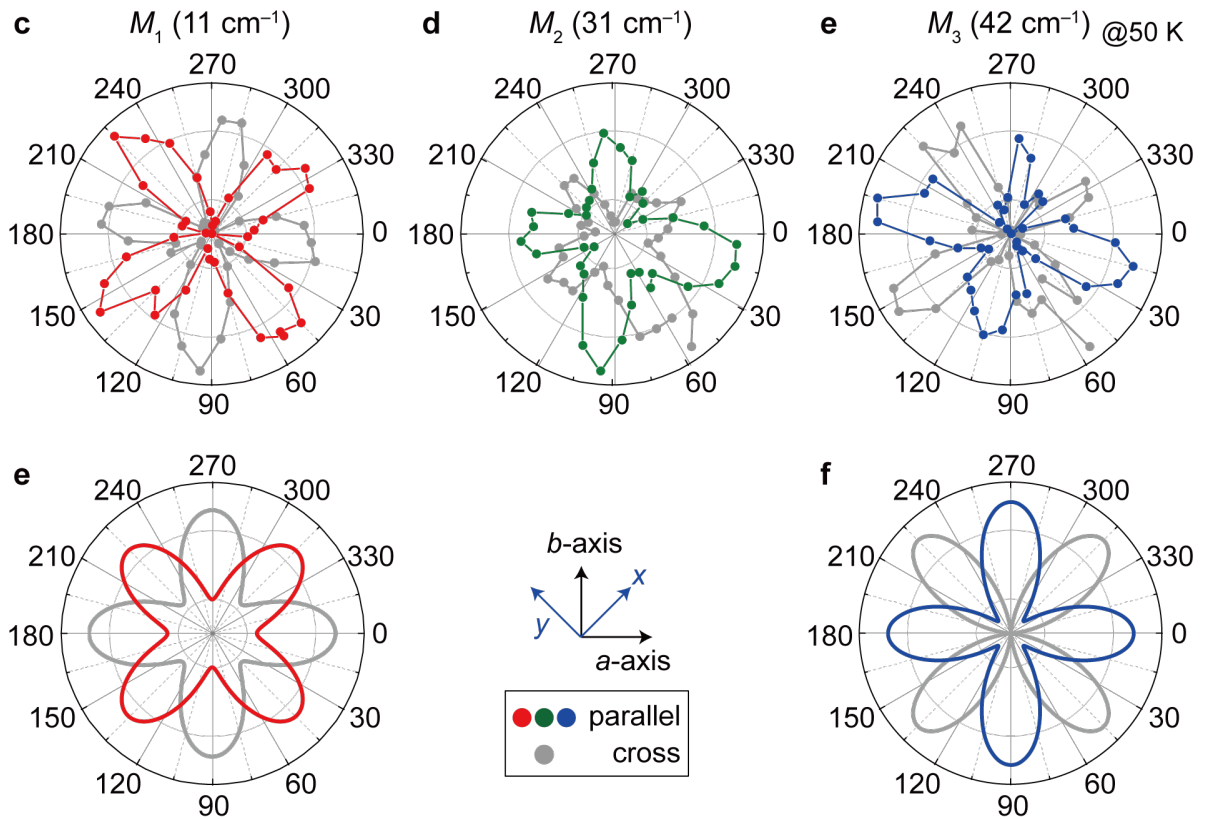
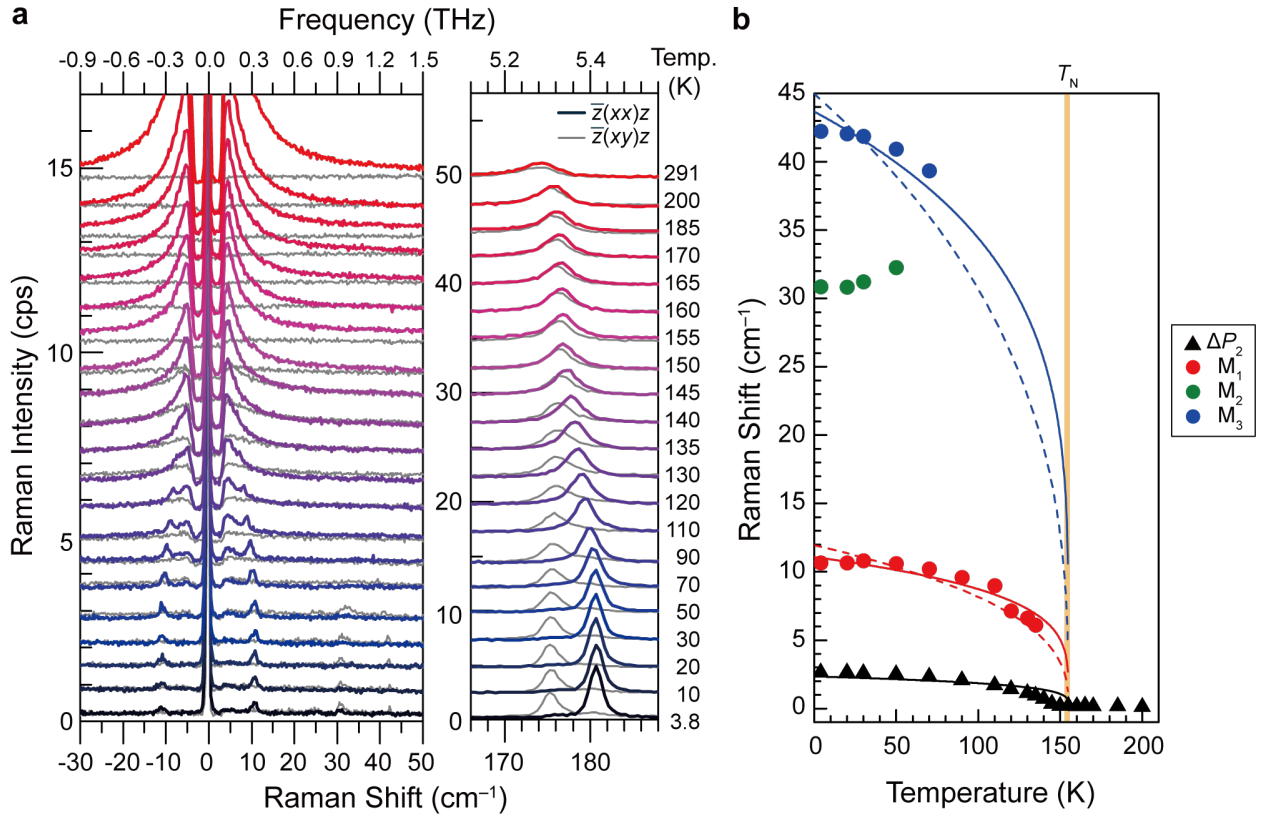


Figure 2. Low-frequency Raman spectra of bulk NiPS₃. a) Temperature dependence of the polarized Raman spectra of bulk (~170 nm) NiPS₃. The colored spectra are measured in $z(xx)\bar{z}$ configuration and the grey spectra in $z(xy)\bar{z}$. At low temperatures, M₁ is observed in $z(xx)\bar{z}$, whereas M₂ and M₃ are observed in $z(xy)\bar{z}$. The splitting (ΔP_2) of the mode at ~180 cm⁻¹ for the two polarizations indicates antiferromagnetic ordering.¹⁹ b) Temperature dependence of the M₁, M₂, M₃, and ΔP_2 . The extrapolated fitting curves for XY (solid) and Heisenberg (dashed) models are shown. c,d,e) Polarization dependence of the intensities of M₁, M₂, and M₃ in the parallel (red, green, blue) and the cross (grey) polarization configurations, respectively. e) Calculated polarization dependence for the red spin-exchange paths in Figure 1. The red (grey) trace is for the parallel (cross) polarization configuration. f) Calculated polarization dependence for the blue spin-exchange paths in Figure 1. The blue (grey) trace is for the parallel (cross) polarization configuration.

Since M₂ and M₃ are too weak in few-layer samples, we mainly analyzed M₁ for the few-layer cases. This peak's excitation-laser-wavelength dependence was surveyed (Figure S2), and it appears strongest for the excitation wavelength of 632.8 nm (1.96 eV), probably due to the resonance with the optical gap of NiPS₃ at 1.8 eV.³⁰ For all the data presented below, we used the 632.8-nm excitation. Figure 2b shows the temperature dependence of M₁, M₂, M₃, and ΔP_2 . The solid curves show the temperature dependence of $[1 - T / T_N]^\beta$ with the exponent β of 0.23 for the XY model,³¹ whereas the dashed curves for the 3-dimensional Heisenberg model³² with β of 0.369 do not show similar agreement. The close agreement with the XY model ascertains that M₁ and M₃ correlate with the antiferromagnetic ordering. Recent magneto-optical measurements on bulk NiPS₃ also indicated that M₁ and M₃ are of magnetic origin.³³ On the other hand, the frequency of M₂ increases with temperature, which was also observed in the previous pump-probe data.²⁶ This indicates that M₂ is not of the same origin as M₁ and M₃. We note that there is a suggestion that M₂ is due to a zone-folded phonon.³⁴

Figure 2c shows the polarization dependence of M_1 measured in the parallel- (red) and cross- (grey) polarization configurations. In parallel (cross) polarization, the analyzer for the scattered photon is set in the direction parallel (cross) to the polarization of the incident photons, and the relative angle between the incident polarization and the crystal axes was rotated. Here, 0° corresponds to the a -axis direction of the crystal. The polarization behaviors of M_2 or M_3 are opposite to that of M_1 (Figure 2d,e), exhibiting correlations with the underlying crystal symmetry. Given the same magnon nature of both M_1 and M_3 , this completely different polarization dependence is most unexpected. To say the least, this observation contradicts the classic theory on light scattering by magnons by Fleury and Loudon,²⁸ which predicts that the light scattering by one magnon is purely antisymmetric, and the one-magnon Raman scattering vanishes in parallel polarization, regardless of the directions of the incident and scattered wave vectors.²⁸ Their predictions are incompatible with our experimental data, which strongly depend on the crystal structure and are clearly not antisymmetric. Therefore, we are led to develop our own theoretical model to explain the experimental results.

Theoretical Analysis on Raman Selection Rule. Shastry and Shraiman³⁵ studied the Raman scattering of Mott-Hubbard systems based on the tight-binding one-band Hubbard model. In their approach, the basic mechanism for the magnetic Raman scattering is the photon-induced spin super-exchange, and the electron-photon interaction is described by the electron hopping Hamiltonian multiplied by the Peierls phase: (spin indices suppressed below)

$$H_{\text{hop-em}} = c_{\mathbf{R}_i, \alpha}^\dagger t_{ij}^{\alpha\gamma} \exp\left(-i \frac{e}{\hbar c} \int_{\mathbf{R}_j}^{\mathbf{R}_i} \mathbf{A}(\mathbf{r}) \cdot d\mathbf{r}\right) c_{\mathbf{R}_j, \gamma}, \quad (1)$$

where \mathbf{R}_i indicates the position of the i -th lattice site, and α, γ denote general quantum numbers such as orbitals. $c_{\mathbf{R}_i \alpha}^\dagger$ is the electron creation operator at the site \mathbf{R}_i with quantum number α . $t_{ij}^{\alpha\gamma}$ is the hopping amplitude of the tight-binding model, and $\mathbf{A}(\mathbf{r})$ is the vector potential of the photon. The photon polarization is directly coupled to the crystal structure in this formulation. They then derived an effective Hamiltonian for Raman scattering by magnetic excitation by treating the electron-photon coupling perturbatively in the second order within the framework of strong coupling expansion of super-exchange. Their result, Equation 8 of Ref. ³⁵, (a missing term is inserted below) is given by

$$H_{\text{eff}} = \sum_{\mathbf{R}} \left(\frac{1}{4} - \mathbf{S}_{\mathbf{R}} \cdot \mathbf{S}_{\mathbf{R}+\boldsymbol{\mu}} \right) \left(\frac{t^2}{U - \hbar\omega_{\text{incoming}}} + \frac{t^2}{U + \hbar\omega_{\text{scattered}}} \right) [\mathbf{A}^{\text{scattered}} \cdot \boldsymbol{\mu}] [\mathbf{A}^{\text{incoming}} \cdot \boldsymbol{\mu}], \quad (2)$$

where $\boldsymbol{\mu}$ is a vector connecting neighbors and $\mathbf{S}_{\mathbf{R}}$ is a spin-1/2 operator at site \mathbf{R} . U is the on-site Coulomb repulsion, and t is the hopping parameter of the one-band Hubbard model, respectively. $\omega_{\text{incoming (scattered)}}$ is the frequency of the incoming (scattered) phonon. It is to be noted that, unlike the classic theory of Fleury and Loudon, the coupling between polarization and crystal structure is now explicit in this new derivation. Clearly, the scattering is no longer *antisymmetric* under the interchange of the polarizations of incoming and scattered photons. However, their result, Eq. (2) based on one-band Hubbard model, cannot yet be directly applied to our case of NiPS₃, mainly due to the differences in the valency of Cu and Ni and the crystal structure.

Here, we recall the previous theoretical work by Koshibae, Ohta, and Maekawa on NiO₂.³⁶ Their tight-binding Hamiltonian can be adapted to NiPS₃ by modifying the underlying crystal structure. Our goal is to derive the magnetic Raman scattering Hamiltonian based on the adapted

Hamiltonian in the framework of Shastry and Shraiman's approach. Considering the complexity of NiPS₃, we seek a tractable minimal model which can describe some features of magnetic excitations. We presume the essential elements to be (1) hopping between Ni and S ions, (2) on-site Coulomb repulsion of Ni ions, and (3) spin-orbit interaction, which is needed for the single-ion magnetic anisotropy responsible for the planar spin configuration.³⁷ We ignore (1) trigonal distortion, (2) Coulomb repulsion and spin-orbit interaction of S ions, (3) direct hopping between Ni ions and between S ions, and (4) all inter-site Coulomb repulsions. It turns out that the qualitative feature of non-antisymmetric scattering polarization dependence can be understood by taking the Ni-S hopping and Ni on-site Coulomb repulsion on the qualitative consistency level. Unfortunately, the inclusion of other elements, in particular the spin-orbit interaction and the trigonal distortion,³⁸⁻⁴¹ render the analytic calculations almost impossible. Evidently the above-ignored elements can play important roles in a more complete description of magnetic excitations.

The basic structure of the effective magnon scattering Hamiltonian obtained from the tight-binding model adapted for NiPS₃ is

$$\hat{H}_{\text{basic}} = P_0 \hat{H}_{\text{e-photon}} \hat{G} \hat{H}_{\text{hop}} \hat{G} \hat{H}_{\text{hop}} \hat{G} \hat{H}_{\text{e-photon}} P_0, \quad (3)$$

where P_0 is the projector onto the subspace of empty S ion holes and Ni spin-triplet states with the energy E_0 , and \hat{G} is the resolvent for the complementary space of P_0 (see Methods). The spins can be exchanged in *two distinct mechanisms: via doubly occupied Ni ion or via doubly occupied S ion*. On top of this, the edge-sharing crystal structure allows several spin exchange paths, depending on the mechanism. The scattering polarization dependence can be extracted from Eq. (3) by reorganizing electron operators in the form of a spin operator (with spin 1). (We mention that the spin-orbit interaction is not considered for the computation of the effective Hamiltonian.)

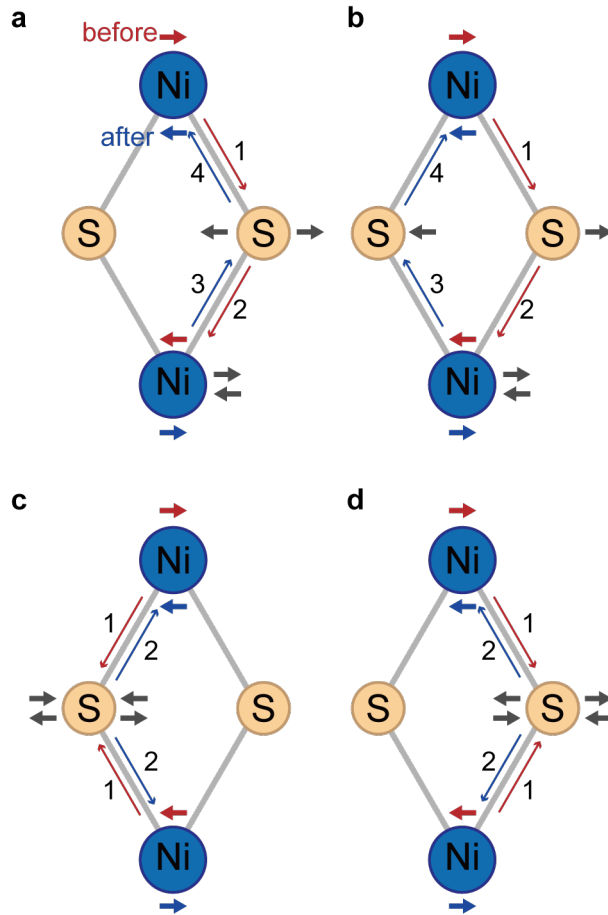


Figure 3. Schematics of typical spin-exchange in NiPS₃ for the opposite-spin pair indicated by the blue ellipse in Figure 1. Spin is exchanged via the doubly occupied Ni ion (a, b) or the doubly occupied S ion (c,d), respectively. The thick red and blue arrows indicate the electron spin before and after the spin-exchange, respectively. The thick gray arrows indicate the spins of the intermediate states. The thin red and blue arrows between Ni and S ions indicate the forward and return paths, respectively. For spins at a doubly occupied Ni ion, there are two possible return paths: either hopping to the right (a) or the left (b) S ion.

Figure 3 illustrates the spin exchange mechanism for the opposite-spin pair (marked by blue ellipse in Figure 1). Spin is exchanged via doubly occupied Ni or S ions. There are four possible exchange paths (and their equivalents). For example, in Figure 3a, the electron with right-spin in

the upper Ni ion is scattered to the nearby Ni ion with left-spin. From this doubly occupied Ni ion, an electron with left-spin is returned to the upper Ni ion, completing the spin exchange. For the parallel-spin pair (marked by red ellipses in Figure 1), the overall exchange mechanism is similar with the consideration of multiple orbitals in the doubly occupied Ni or S ions. Note that Figure 3 depicts spin-1/2 exchanges, whereas the spin-1 scattering Hamiltonian (Eq. (9) in Materials and Methods) is obtained by considering e_g multiple orbitals and the Wigner-Eckart theorem (see Supporting Information Eq. (S13) and accompanying explanation).

By combining the contributions for a ferromagnetic Ni ion pair, we can obtain a polarization dependence consistent with M_1 (Figure 2e). In contrast, those from an antiferromagnetic pair are consistent with M_3 (Figure 2f). This comparison shows that the spin exchange scattering paths in the zigzag direction (same spins) dominate the M_1 magnon. Those in the armchair (opposite spins) directions are more critical for the M_3 magnon. We stress that this observation is an entirely new piece of information. Usually, the super-exchange generates antiferromagnetic coupling between spins. However, from the viewpoint of the effective scattering Hamiltonian, the sign of the *effective* exchange constant can be both positive and negative, as can be seen in Eq. (2). For more rigorous calculations, one has to consider the complicated sign patterns of the hopping amplitude between d orbital of Ni ion and p orbital of S ion in trigonally distorted octahedron geometry and the spin-orbit interaction which can be responsible for the zigzag planar spin configuration. This is well beyond the scope of the current work.

Raman Spectroscopy on Few-layer NiPS₃. Figure 4a shows the dependence of M_1 at 50 K on the number of layers along with that of a bulk sample. The polarization was chosen so that the

intensity of M_1 is at its maximum. The full set of spectra is shown in Figure S3 and S4. The evolution of the interlayer breathing mode (■) with the layer number is consistent with the previous report.¹⁹ M_1 is observed for thicknesses down to 2L, whilst it is absent from the spectrum of 1L. This is also consistent with the suppression of the magnetic ordering¹⁹ in 1L NiPS₃ and serves as additional evidence that this peak is indeed a result of the antiferromagnetic ordering.

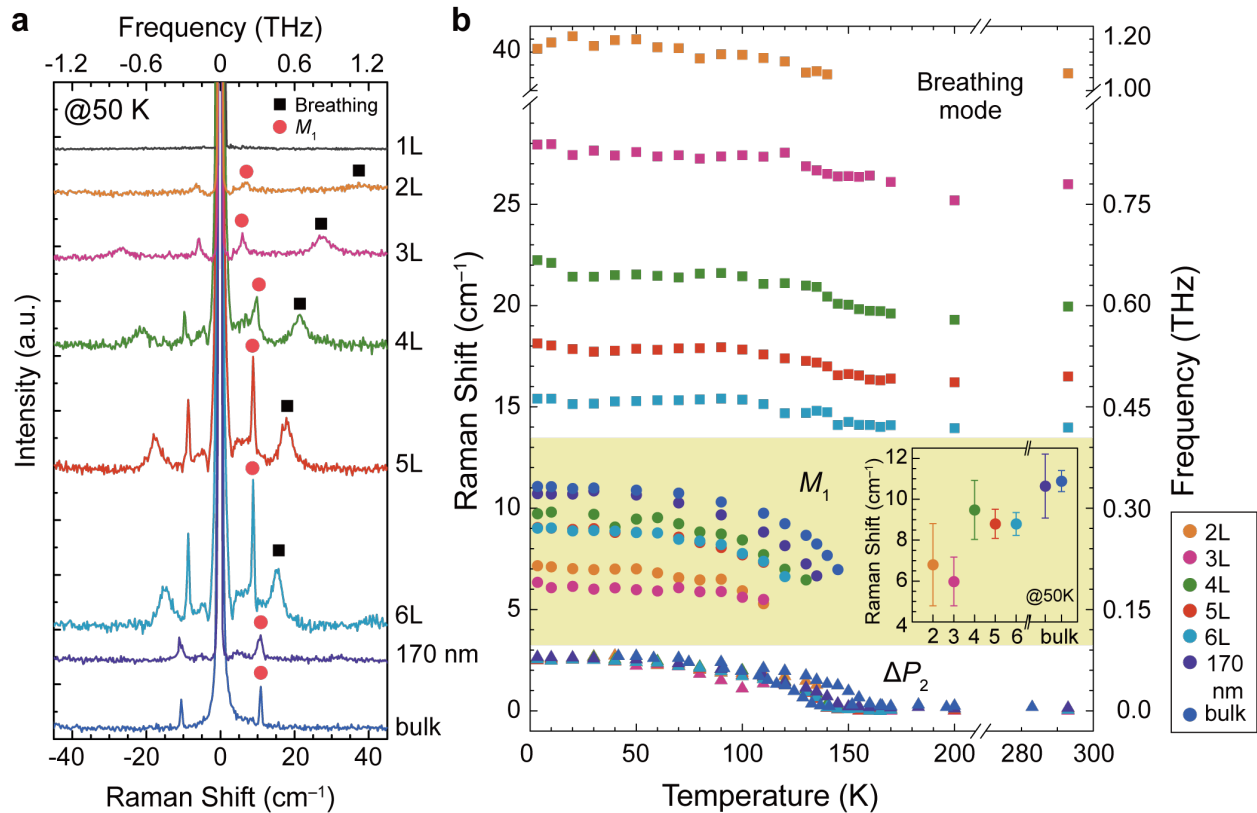


Figure 4. Temperature dependence of low-frequency Raman modes of few-layer NiPS₃. a) Layer-number dependence of low-temperature Raman spectra. The M_1 and interlayer breathing modes are marked with red circles and black square symbols, respectively. b) Temperature dependence of the Raman modes in the low-frequency range for different numbers of layers. ΔP_2 is also plotted for each number of layers for comparison. The inset shows the thickness dependence of the M_1 magnon mode.

Unfortunately, M_2 and M_3 are too weak to be resolved reliably in few-layer samples, so we cannot examine their thick dependence in detail. But M_1 shows a clear dependence on the number of layers: the peak redshifts as the thickness decreases, although the redshift does not scale linearly with the thickness. Potential origins for the decrease in the peak frequency are discussed below. The temperature dependences of M_1 for few-layer samples are similar to that for the bulk sample and can be described with the same exponent of 0.23 (Figure 4b and Figure S5a). For thinner samples, M_1 becomes unresolved as the temperature increases toward T_N because of the enhanced QES signal near the magnetic transition temperature¹⁹ (see Figure S4). The intensity of M_1 tends to increase with temperature up to ~ 40 K and then decrease again when the temperature is further raised beyond ~ 80 K (Figure S5b). This temperature dependence is not understood yet. Interestingly, the breathing modes also blueshift below T_N . This is because the additional magnetic interaction between the layers below T_N increases the ‘spring constant’ between the layers.

Inelastic Neutron Scattering Analysis. We complement our analysis with the INS measurement results to better understand the low-energy magnetic excitations. Previous INS studies successfully captured the overall magnon-spectra of NiPS₃ within the $[H, K, 0]$ plane (in reciprocal lattice units, r.l.u.), including the gapped low-energy magnon mode at approximately 5 meV (e.g., see $Q = [0, 1, 0]$ in Figure 5a, where Q denotes a momentum).^{23, 24} Notably, this energy corresponds to the excitation energy of the M_3 mode. However, the spectra in the $[H, K, 0]$ plane failed to identify a signal below 5 meV, i.e., the M_1 mode. After having obtained the Raman data shown earlier, we examined our data more carefully and observed a clear magnon dispersion down to approximately 1.5 meV at the magnon zone centers on the $[H, K, 1]$ plane.

Figure 5b shows such observations at $Q = [0, 1, 1]$, and a similar spectrum at $Q = [1/2, 1/2, 1]$ – an equivalent Q position to $[0, 1, 1]$ but simply corresponding to a different magnetic domain – is shown in Supporting Information (Figure S6). These results suggest that M_1 (1.5 meV or 12 cm^{-1}) and M_3 (5 meV or 40 cm^{-1}) are the single-magnon excitations at the Γ point. On the other hand, there is no clear indication of a magnetic excitation corresponding to the energy of M_2 (3.8 meV). Thus, the M_2 mode is not likely to be a single-magnon excitation. This is consistent with a conventional dipole spin-wave theory, which yields only two magnon eigenvalues at the Γ point as two spin sublattices are present in NiPS_3 .

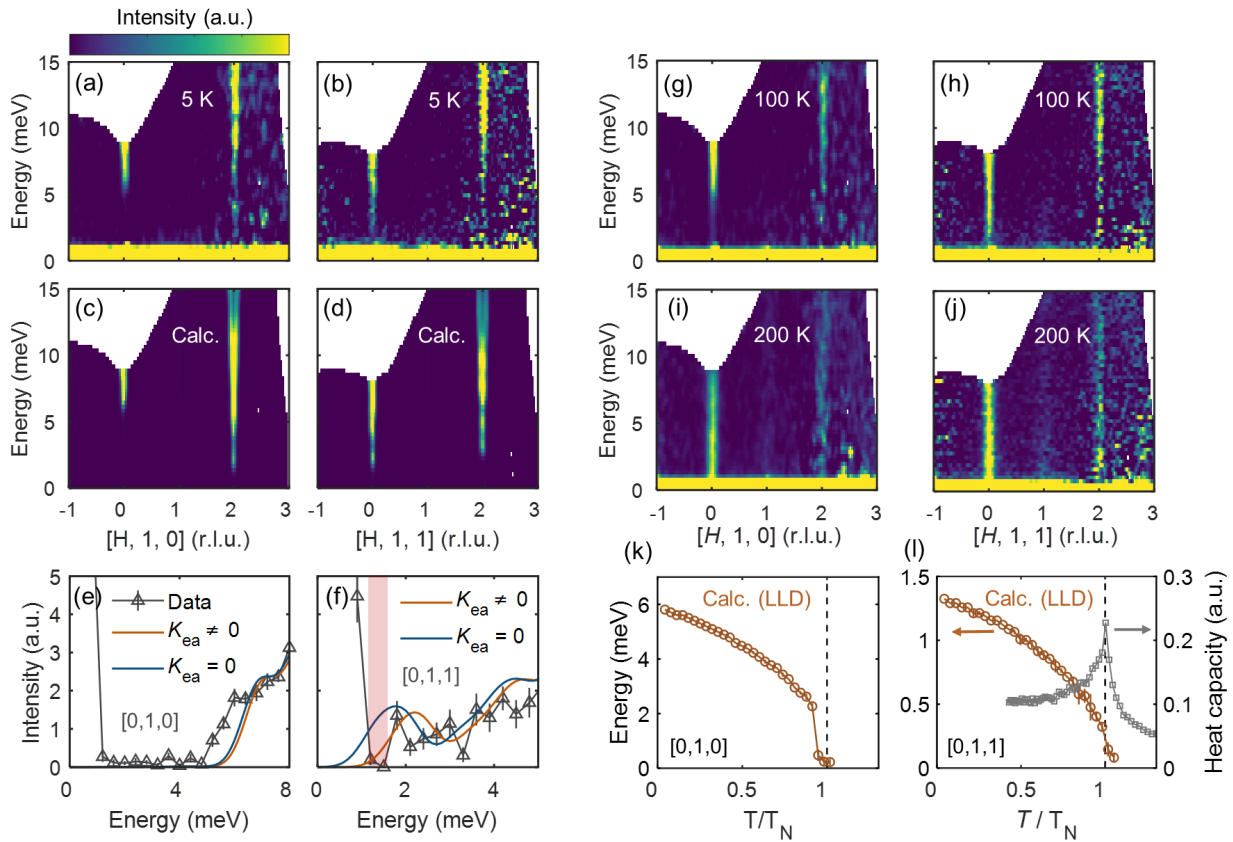


Figure 5. Low-energy magnon spectra of NiPS_3 . a,b) The magnon spectra measured by inelastic neutron scattering (INS) at 5 K. c,d) The magnon spectra calculated by linear spin-wave theory (LSWT, see Methods), each corresponding to (a) and (b), respectively. e,f) The constant- Q cuts of the INS data in (a) and (b) at $Q = [0, 1, 0]$ and $[0, 1, 1]$ (r.l.u.), each demonstrating gapped magnon

modes at ~ 5 meV and ~ 1.5 meV. Orange and blue solids curves are the LSWT calculation results with and without easy-axis anisotropy K_{ea} , respectively. The simulation results in (c)-(f) include instrumental resolution and experimental binning width effects. g,h,i,j) The magnon spectra measured at 100 K ($< T_N$) and 200 K ($> T_N$). k,l) The temperature dependence of the magnon energy gap at $\mathbf{Q} = [0, 1, 0]$ and $\mathbf{Q} = [0, 1, 1]$ calculated by Landau-Lifshitz dynamics (LLD) simulation (see Methods). Grey data points are the heat capacity calculated from the same simulation, showing the transition temperature of the theoretical NiPS₃ spin system.

For a better understanding on the two gapped modes assigned as M_1 and M_3 , we calculated the theoretical magnon spectra of NiPS₃ using the linear spin-wave theory (LSWT, see Methods). The spin Hamiltonian used in our calculations was based on previous studies:^{23, 24}

$$H = J_n \sum_{(i,j)_n} \mathbf{S}_i \cdot \mathbf{S}_j + K_{ep} \sum_i (S_i^z)^2 + K_{ea} \sum_i (S_i^x)^2 \quad (4)$$

where J_n and $(i,j)_n$ denote the exchange constant and the site indices for the n^{th} nearest neighbors, and K_{ep} (> 0) and K_{ea} (< 0) are the magnitudes of easy-plane (the a - b plane) and easy-axis ($x // a$ -axis) anisotropy, respectively. We adopted the same exchange and single-ion anisotropy parameters as those in Ref. 24. As shown in Figure S7, Supporting Information, this model successfully yields magnon eigenvalues of 1.28 meV ($= 10.32 \text{ cm}^{-1}$) and 5.97 meV ($= 48.15 \text{ cm}^{-1}$) at the Γ point, each aligning with the energy of M_1 and M_3 . Notably, each eigenmode originates from non-zero K_{ea} and K_{ep} in Eq. (4), respectively, indicating that the formation of M_1 (M_3) is associated with the easy-axis (easy-plane) anisotropy at the Ni sites.

Our dynamical structure factor calculations further reveal that only the 5.97 meV mode is visible at $\mathbf{Q} = [0, 1, 0]$ (Figure 5c or Figure S7), consistent with our observation (Figure 5a). On the other hand, both modes possess sizable structure factor and thus should appear together at $\mathbf{Q} =$

[2, 1, 0] or [0, 1, 1] (Figure S7). However, such a double-gap structure anticipated from our calculation does not manifest clearly in the INS spectra, as depicted in Figure 5a and b. The reason behind this discrepancy is the effect of momentum resolution and experimental bin width that are particularly significant in the low-energy excitation spectra of NiPS₃, as described in the Introduction or Ref. ²⁴. Figure 5c,d show the calculated magnon spectra with such resolution effects taken into account, indeed bearing strong similarities to the measured INS spectra (Figure 5a,b).

The presence of M₁ in the INS data is more evident in its constant-**Q** cut at **Q** = [0, 1, 1] (Figure 5f). While a quasi-elastic background signal dominates the spectrum for $E < 1$ meV, the data points within a red-shaded region in Figure 5f indicate an energy gap of approximately 1.5 meV (= 12 cm⁻¹). This gapped feature was further verified by comparing it with the calculation from $K_{ea} = -0.01$ meV and $K_{ea} = 0$, each representing a gapped and gapless magnon model, respectively. Both the gapped (solid orange curve in Figure 5f) and gapless (solid blue curve in Figure 5f) magnon models result in a gapped feature due to the significant resolution effect mentioned earlier. However, the gapless magnon model fails to explain the vanishing intensity near 1.5 meV (the red-shaded region). This again supports our interpretation that M₁ corresponds to a gapped single-magnon excitation stemming from K_{ea} .

Temperature dependence of these low-energy magnetic excitations, examined through INS and theoretical calculations, not only corroborates the single-magnon nature of M₁ and M₃ but also reveals a non-trivial character beyond semi-classical spin dynamics theory. Figure 5g-j show the measured INS spectra at 100 and 200 K. Indeed, increased thermal fluctuations cause the M₁ and M₃ magnon modes to get subdued significantly at higher temperatures (Figure 5g,h) and eventually close their energy gap for $T > T_N$ (Figure 5i,j), similar to the Raman spectroscopy result (Figure

2). The corresponding spin dynamics simulations at finite temperatures were conducted using semi-classical Landau-Lifshitz dynamics (LLD) (see Methods). Similar to the LSWT calculation, we employed the spin Hamiltonian described in Equation 4 for this simulation. The results shown in Figure 5k and l present that the energy gaps behave like an order parameter of the phase transition at T_N . However, the LLD simulation indicates a more gradual increase in magnon energy below T_N (Figure 5l) compared to the observed behavior of M_1 . Hence, while our spin model adequately describes the presence of the M_1 magnon mode and its qualitative dissipation by thermal fluctuations, M_1 possesses additional characteristics not captured by the semi-classical spin dynamics theory. Importantly, this aligns with the intensity anomaly of the M_1 peak observed on the $[H, K, 0]$ plane, which cannot be modelled accurately by LSWT.²⁴

The observed thickness dependence of M_1 warrants further discussion, particularly with regards to its relevance to the easy-axis anisotropy (K_{ea}) in Eq. (4). Phenomenologically, the sudden decrease in M_1 's energy in bi- and tri-layer NiPS₃ can be interpreted as a reduction in either $|K_{ea}|$ or the spin expectation value $\langle S \rangle$ (i.e., the magnitude of the ordered moment). While a change in $\langle S \rangle$ would arise to some extent due to the enhanced fluctuations in reduced dimensions, the change in $|K_{ea}|$ is also expected to take place in the nearly 2D limit, given its origin inferred from symmetry arguments. While each layer in NiPS₃ conforms to trigonal symmetry (e.g. a honeycomb lattice), the monoclinic stacking in the bulk structure lowers the entire symmetry of the system to two-fold. Thus, K_{ea} , which is not compatible with the trigonal geometry of a single isolated layer, is presumably induced by the symmetry lowering by the monoclinic inter-layer environment. However, in bi- and tri-layer NiPS₃, a significant portion of the sample (e.g. 33 % in bi-layer nanoflakes) interfaces with vacuum or substrate instead of another NiPS₃ layer. Thus, the influence of monoclinic stacking is expected to decrease a lot, leading to a sizable change in $|K_{ea}|$. Notably,

such modifications driven by reduced dimensions can only be elucidated through spin dynamics measurements of atomically-thin flakes – an analysis beyond the reach of an INS technique. On the other hand, the evolution of M_3 with decreasing thickness is anticipated to be less dramatic, as the easy-plane anisotropy K_{ep} , the source of M_3 , is compatible with the trigonal symmetry inherent to each layer. Finally, unlike M_1 and M_3 we failed to observe any feature in our inelastic neutron scattering data that can be associated with the M_2 peak in the Raman data: which reinforces that it is more likely to be of phonon origin.

CONCLUSION

NiPS₃ is arguably the most exciting vdW antiferromagnet with several noticeable features, including the highly narrow and linear polarized exciton peak. It is believed that in NiPS₃, all three degrees of freedom: spin, charge, and lattice, are entangled with one another. Using the high-resolution ultralow-frequency Raman technique, we succeeded in measuring low-lying magnons down to bilayer NiPS₃, which has so far remained in the realm of the unachievable despite its fundamental importance. By comparing with inelastic neutron scattering data, we established the magnon nature of these low-energy modes beyond doubt. The Raman signals due to these magnons exhibit striking polarization dependences that according to our new theoretical model, are intricately related to the spin-exchange scattering paths of these magnons. Our work opened the door to a new way of studying spin dynamics down to atomically thin layers of vdW magnets, which can be applied to many vdW and other 2D magnets such as FePS₃ which also shows magnon signals in the Raman spectrum.⁴²

MATERIALS AND METHODS

Sample Preparation and Characterization. NiPS₃ crystals were grown by the chemical vapor transport (CVT) method, as explained in Ref. ⁴³ and Ref. ²⁴. Inside an argon-filled glove box, elemental powders (purchased from Sigma-Aldrich) of nickel, phosphorus, and sulfur were weighed and mixed in a stoichiometric ratio. Few-layer NiPS₃ samples were mechanically exfoliated onto 285-nm SiO₂/Si substrates using scotch tape from single-crystal flakes. The thickness of each sample was determined by the optical contrast of microscope images and Raman spectroscopy. The Néel vector of the antiferromagnetically ordered phase was determined from the polarization dependence of the magnetic exciton photoluminescence signal at 1.48 eV.⁴⁴

Raman Spectroscopy. The temperature-dependent low-frequency Raman spectra of bulk and few-layer NiPS₃ were measured in a micro-measurement system using a closed-cycle He cryostat (Montana instruments). The laser beam was focused to a focus of ~ 1 μm in diameter by a 40 \times microscope objective lens (0.6 N.A.) with a power below 100 μW to avoid damage to the sample, and the scattered light was collected and collimated by the same objective. The excitation light was the 632.8-nm line of a He-Ne laser except for the comparison of the excitation wavelengths in Figure S1. To access the low-frequency range below 100 cm^{-1} , volume holographic filters (OptiGrate) were used to clean the laser lines and to reject the Rayleigh-scattered light. For parallel (cross) polarization, the analyzer angle was set such that photons with polarization parallel (cross) to the incident polarization pass through. Another achromatic half-wave plate was placed in front of the spectrometer to keep the polarization direction of the signal entering the spectrometer constant with respect to the groove direction of the grating. The Raman signal was dispersed by a Jobin-Yvon Horiba iHR550 spectrometer (2,400 grooves/mm) and detected with a liquid-nitrogen-cooled back-illuminated charge-coupled-device (CCD) detector.

Single-Crystal INS Measurements. We conducted the inelastic neutron scattering (INS) experiment using the SEQUOIA time-of-flight spectrometer^{45,46} at the Spallation Neutron Source (Oak Ridge National Laboratory, USA).⁴⁷ For the experiment, we co-aligned 26 single-crystal pieces (~ 2.41 g) of NiPS₃ on three circular aluminum plates (see Ref. ²⁴). We collected the data at 5, 100, and 200 K with three incident energies: 28, 60, and 100 meV. The sample was mounted in the geometry of the (H K 0) scattering plane and was rotated during the measurement to collect the spin waves over the full Brillouin zone. A background signal was estimated by measuring an empty sample holder's signal and was subtracted from our INS data. We used Horace software for the data analysis.⁴⁸ The data were symmetrized based on the in-plane mirror operation: that is, [H, K, L] \rightarrow [H, -K, L]. The data integration range of the plots in Figure 5a and b and Figure 5g and h is ± 0.05 r.l.u. for [0, K, 0] direction and ± 0.15 r.l.u. for the direction perpendicular to the [H, K, 0] plane. The integration range of the constant-Q cuts in Figure 5e and f is ± 0.04 r.l.u. for [H, 0, 0] and [0, K, 0] directions and ± 0.15 r.l.u. for the direction perpendicular to the [H, K, 0] plane.

THEORETICAL CALCULATIONS

Spin-Wave Calculations. We calculated the magnon eigenvalues and INS cross-sections of NiPS₃ using linear spin-wave theory. For this calculation, we used the SpinW library.⁴⁹ For a precise comparison with the measured INS spectra, we applied the instrumental resolution and the effect of experimental bin width to our simulation. The calculation results are shown in Figure 5c-f and Figure S7. We simulated the spin system based on Landau-Lifshitz dynamics (LLD) to calculate the low-energy magnon modes at finite temperatures. This was done using the calculation package Su(n)ny, whose details can be found in Refs. ^{50, 51, 52}. For bulk NiPS₃, we prepared a

100×100×2 supercell (80,000 Ni²⁺ sites) and sampled its time evolution governed by LLD. To calculate the magnon mode at ~1.28 meV (5.97 meV), a Langevin time step and a damping constant were set to $dt = 0.2/J_3 = 0.0143 \text{ meV}^{-1}$ ($dt = 0.1/J_3 = 0.0072 \text{ meV}^{-1}$) and $\lambda = 0.1$, respectively. The sampling was begun after evolving the system over 4,000~8,000 Langevin time steps for equilibration, which depends on the length of a single Langevin time step. Based on the sampled results, we calculated the dynamical structure factor of the spin system and analyzed the energy of a magnon peak at $\mathbf{Q} = [0, 1, 0]$ and $[0,1,1]$ (r.l.u.). We repeated this calculation 10 times at each temperature and used the averaged values. The result is shown in Figure 5k and l.

Calculation of Polarization Dependence. First, let us describe the tight-binding model Hamiltonian for NiPS₃. Adopting the hole picture for the electronic states of Ni and S ions, the vacuum is the filled 3d levels of Ni and 2p levels of S. Then Ni ions will have two holes in e_g orbitals ($x^2 - y^2$, $3z^2 - r^2$, denoted by 0, 1) in the spin-triplet state. Hund's rule on-site Coulomb interaction is implicitly assumed to enforce the spin-triplet ground state at each Ni ion (this is implemented by Wigner-Eckart theorem, see chapter 7 of Ref. ⁵³ and Ref. ³⁶). The tight-binding Hamiltonian consists of on-site terms and hopping terms. Recall that the photon couples to an electron through the hopping terms.

$$\hat{H} = \hat{H}_{\text{on-site}} + \hat{H}_{\text{hop}} + \hat{H}_{\text{e-photon}}. \quad (5)$$

The on-site Hamiltonian consists of the site energy of Ni and S ions, Hubbard U repulsion, inter-orbital repulsion, and spin-orbit interaction. The detailed expressions are in Supplementary Information. All parameters of these Hamiltonians should be regarded to be phenomenological. The on-site spin-orbit interaction is *not* going to be included in the computation of effective scattering Hamiltonian for the sake of simplicity. *This is a grave approximation* and can be potentially problematic.

Next, take the crystal structure into account. Ni ion sites form a honeycomb lattice. Also, each Ni ion sits at the center of a hexagon formed by S ions. This crystal structure is edge-sharing so that each S ion is shared by two neighboring Ni ions; hence, it allows *multiple spin super-exchange paths*. To derive the effective Hamiltonian, we apply the strong coupling expansion of super-exchange in the second order of $\hat{H}_{\text{e-photon}}$ (the second order light scattering) and the second order of \hat{H}_{hop} (for the intermediate states created by photon involving the doubly occupied states). The basic structure of the effective magnon scattering Hamiltonian is

$$\hat{H}_{\text{basic}} = P_0 \hat{H}_{\text{e-photon}} \hat{G} \hat{H}_{\text{hop}} \hat{G} \hat{H}_{\text{hop}} \hat{G} \hat{H}_{\text{e-photon}} P_0, \quad (6)$$

where P_0 is the projector onto the subspace of empty S ion holes and Ni spin-triplet states with the energy E_0 .

$$\hat{G} = \frac{\text{Id} - P_{E_0}}{E_0 - \hat{H}_{\text{on-site}}} \quad (7)$$

is the resolvent for the complementary space of P_0 (namely the intermediate states with higher energies). After reorganizing the electron operators appearing in Equation 6 in terms of spin operators we can find the effective Hamiltonian of the magnetic Raman scattering analogous to Equation 2.

In the perturbative expansion Equation 6, the spins of two neighboring Ni ions (located at \mathbf{R} and \mathbf{R}') can be exchanged with photon absorption/emission. The spins are exchanged along paths via two shared S ions whose positions are designated as follows:

$$\mathbf{R} + \boldsymbol{\delta}_1 = \mathbf{R}' + \boldsymbol{\delta}'_1 = \text{S-ion 1}, \quad \mathbf{R} + \boldsymbol{\delta}_2 = \mathbf{R}' + \boldsymbol{\delta}'_2 = \text{S-ion 2} \quad (8)$$

where $\boldsymbol{\delta}$ is a vector connecting a Ni ion to the surrounding S ion in the hexagon.

The spins can be exchanged in *two distinct mechanisms: via doubly occupied Ni ion or via doubly occupied S ion*. On top of this, the edge-sharing crystal structure allows several spin exchange paths depending on a mechanism. Since the parameters of the tight-binding Hamiltonian are unknown, the relative magnitude/sign of the amplitudes of these two mechanisms are essentially arbitrary. We will further assume that the amplitudes are identical for a given exchange mechanism except for the photon polarization factor. With these provisions, the effective Hamiltonian can be expressed as ($\mathbf{S}_{\mathbf{R}}$ is the Ni spin-1 operator at site \mathbf{R})

$$\hat{H}_{\text{eff, NiPS}_3} = \sum_{\langle \mathbf{R}, \mathbf{R}' \rangle} \mathbf{S}_{\mathbf{R}} \cdot \mathbf{S}_{\mathbf{R}'} [M_{\text{Ni}} \mathbf{C}_{\text{Ni}} + M_{\text{S}} \mathbf{C}_{\text{S}}], \quad (9)$$

where $M_{\text{Ni/S}}$ is the amplitude via doubly occupied Ni/S ion *apart from the polarization factor* $\mathbf{C}_{\text{Ni/S}}$ and $\langle \mathbf{R}, \mathbf{R}' \rangle$ indicates the nearest neighbor pair. The detailed expressions for $M_{\text{Ni/S}}$ are in Supplementary Note 1. The most important polarization factors are as follows ($\hat{\mathbf{q}}_{i,s}$ is the polarization vector of incoming and scattered photons, respectively):

$$\begin{aligned} \mathbf{C}_{\text{Ni}} = & 2(\hat{\mathbf{q}}_i \cdot \delta_1)(\hat{\mathbf{q}}_s^* \cdot \delta_1) + 2(\hat{\mathbf{q}}_i \cdot \delta_2)(\hat{\mathbf{q}}_s^* \cdot \delta_2) + 2(\hat{\mathbf{q}}_i \cdot \delta'_1)(\hat{\mathbf{q}}_s^* \cdot \delta'_1) + 2(\hat{\mathbf{q}}_i \cdot \delta'_2)(\hat{\mathbf{q}}_s^* \cdot \delta'_2) \\ & + 2(\hat{\mathbf{q}}_i \cdot \delta_1)(\hat{\mathbf{q}}_s^* \cdot \delta_2) + 2(\hat{\mathbf{q}}_i \cdot \delta_2)(\hat{\mathbf{q}}_s^* \cdot \delta_1) + 2(\hat{\mathbf{q}}_i \cdot \delta'_1)(\hat{\mathbf{q}}_s^* \cdot \delta'_2) + 2(\hat{\mathbf{q}}_i \cdot \delta'_2)(\hat{\mathbf{q}}_s^* \cdot \delta'_1), \end{aligned} \quad (10)$$

$$\begin{aligned} \mathbf{C}_{\text{S}} = & 2(\hat{\mathbf{q}}_i \cdot \delta_1)(\hat{\mathbf{q}}_s^* \cdot \delta_1) + 2(\hat{\mathbf{q}}_i \cdot \delta_2)(\hat{\mathbf{q}}_s^* \cdot \delta_2) + 2(\hat{\mathbf{q}}_i \cdot \delta'_1)(\hat{\mathbf{q}}_s^* \cdot \delta'_1) + 2(\hat{\mathbf{q}}_i \cdot \delta'_2)(\hat{\mathbf{q}}_s^* \cdot \delta'_2) \\ & + 2(\hat{\mathbf{q}}_i \cdot \delta_1)(\hat{\mathbf{q}}_s^* \cdot \delta_1) + 2(\hat{\mathbf{q}}_i \cdot \delta_1)(\hat{\mathbf{q}}_s^* \cdot \delta_1) + 2(\hat{\mathbf{q}}_i \cdot \delta'_2)(\hat{\mathbf{q}}_s^* \cdot \delta'_2) + 2(\hat{\mathbf{q}}_i \cdot \delta'_2)(\hat{\mathbf{q}}_s^* \cdot \delta'_2). \end{aligned} \quad (11)$$

In principle, we can expand the spin operator of Equation 9 in a magnon basis starting from the microscopic tight-binding Hamiltonian and use the standard Fermi Golden rule to obtain the scattering intensity. Unfortunately, the magnon operators cannot be obtained within our approximation, but the polarization dependence can still be extracted. An immediate comment is in order: the effective Hamiltonian Equation 9 is *isotropic* in spin, starkly contrasting with the observed planar spin configuration. This is to be expected because the spin-orbit interaction is not considered (the inclusion of spin-orbit interaction renders explicit calculations intractable).

Despite these apparent shortcomings, it turns out that the results for the polarization dependence appear to be consistent with the experimental data with a suitable adjustment of relative weight between M_{Ni} and M_S . We point out that the analytical expressions for the exchange constants of the spin Hamiltonian have been obtained in Ref. 36. However, we cannot extract the quantitative values of the exchange constants since the parameters of the multi-orbital tight-binding Hamiltonian are not known.

ASSOCIATED CONTENT

Supporting Information.

The Supporting Information is available free of charge on the ACS Publications website at DOI: 10.1021/acsnano.xxxxxxx.

Calculation of Polarization Dependence; Determination of crystal axes; Low-frequency Raman spectra at 50 K measured by using lasers with different wavelengths; Temperature dependence of polarized Raman spectra for 6L, 5L, 4L, 3L, 2L and 1L NiPS₃; Temperature dependence of M_1 magnon peak and ΔP_2 for few-layer NiPS₃; INS data of NiPS₃ along the momentum contour $[H, 1/2, 1]$ (r.l.u.); INS cross-sections of NiPS₃ at $Q = [0, 1, 0]$ and $[0, 1, 1]$ calculated from linear spin-wave theory and Equation 4 of the main text.

AUTHOR INFORMATION

Corresponding Authors

*E-mail: hyunlee@sogang.ac.kr, jgpark10@snu.ac.kr, hcheong@sogang.ac.kr

Author Contributions

J.-G.P. and H.C. conceived the experiments and supervised the project. J.K. synthesized NiPS₃ samples and characterized them for Raman experiments. W.N., S.O., and H.C. prepared few-layer samples and performed Raman measurements. P.P. grew NiPS₃ single crystal samples and aligned them for the inelastic neutron scattering measurements, which were conducted with A.S. and A.T. H.C.L carried out the theoretical analysis of Raman scattering. All the authors analyzed the data and wrote the manuscript jointly.

Notes

The authors declare no competing financial interest.

ACKNOWLEDGMENT

We acknowledge C. L. Sarkis and M. B. Stone for their help regarding the INS experiment and N. Perkins for helpful discussion. This work was supported by the National Research Foundation (NRF) grant funded by the Korean government (MSIT) (2019R1A2C3006189, 2017R1A5A1014862, SRC program: vdWMRC Center). This research used resources at the Spallation Neutron Source, a U.S. Department of Energy (DOE) Office of Science User Facility operated by the Oak Ridge National Laboratory (ORNL). P. Park acknowledges support by the U.S. Department of Energy, Office of Science, Basic Energy Sciences, Materials Science and Engineering Division. The work at Seoul National University was supported by the Leading Researcher Program of the National Research Foundation of Korea (Grant No. 2020R1A3B2079375). The work by A. Scheie and D.A. Tennant is supported by the Quantum Science Center (QSC), a National Quantum Information Science Research Center of the U.S. Department of Energy (DOE).

REFERENCES

- (1) Onsager, L. Crystal Statistics. I. A Two-Dimensional Model with an Order-Disorder Transition. *Physical Review* **1944**, *65*, 117-149. DOI: 10.1103/PhysRev.65.117.
- (2) Mermin, N. D.; Wagner, H. Absence of Ferromagnetism or Antiferromagnetism in One- or Two-Dimensional Isotropic Heisenberg Models. *Phys Rev Lett* **1966**, *17* (22), 1133-1136.
- (3) Berezinskii, V. Destruction of long-range order in one-dimensional and two-dimensional systems having a continuous symmetry group I. Classical systems. *Soviet Physics JETP* **1971**, *32*, 493-500.
- (4) Kosterlitz, J. M.; Thouless, D. J. Ordering, metastability and phase transitions in two-dimensional systems. *Journal of Physics C: Solid State Physics* **1973**, *6* (7), 1181-1203. DOI: 10.1088/0022-3719/6/7/010.
- (5) *Magnetic Properties of Layered Transition Metal Compounds*; Springer Dordrecht, 1990. DOI: 10.1007/978-94-009-1860-3.
- (6) Bramwell, S. T.; Day, P.; Hutchings, M. T.; Thorne, J. R. G.; Visser, D. Neutron scattering and optical study of the magnetic properties of the two-dimensional ionic rubidium chromium bromide chloride ferromagnets $\text{Rb}_2\text{CrCl}_3\text{Br}$ and $\text{Rb}_2\text{CrCl}_2\text{Br}_2$. *Inorganic Chemistry* **1986**, *25* (4), 417-421. DOI: 10.1021/ic00224a008.
- (7) Cook, A. H.; Edmonds, D. T.; Finn, C. B. P.; Wolf, W. P. Magnetic dipole interactions in dysprosium ethyl sulphate II. Magnetic and thermal properties between 1 °K and the Curie point. *Proceedings of the Royal Society A* **1968**, *306*, 313-334. DOI: 10.1098/rspa.1968.0153.
- (8) Park, J.-G. Opportunities and challenges of 2D magnetic van der Waals materials: magnetic graphene? *Journal of Physics: Condensed Matter* **2016**, *28* (30). DOI: 10.1088/0953-8984/28/30/301001.

- (9) Lee, J. U.; Lee, S.; Ryoo, J. H.; Kang, S.; Kim, T. Y.; Kim, P.; Park, C. H.; Park, J. G.; Cheong, H. Ising-Type Magnetic Ordering in Atomically Thin FePS₃. *Nano Lett* **2016**, *16* (12), 7433-7438. DOI: 10.1021/acs.nanolett.6b03052.
- (10) Gong, C.; Li, L.; Li, Z. L.; Ji, H. W.; Stern, A.; Xia, Y.; Cao, T.; Bao, W.; Wang, C. Z.; Wang, Y. A.; et al. Discovery of intrinsic ferromagnetism in two-dimensional van der Waals crystals. *Nature* **2017**, *546* (7657), 265-269. DOI: 10.1038/nature22060.
- (11) Huang, B.; Clark, G.; Navarro-Moratalla, E.; Klein, D. R.; Cheng, R.; Seyler, K. L.; Zhong, D.; Schmidgall, E.; McGuire, M. A.; Cobden, D. H.; et al. Layer-dependent ferromagnetism in a van der Waals crystal down to the monolayer limit. *Nature* **2017**, *546* (7657), 270-273. DOI: 10.1038/nature22391.
- (12) Burch, K. S.; Mandrus, D.; Park, J. G. Magnetism in two-dimensional van der Waals materials. *Nature* **2018**, *563* (7729), 47-52. DOI: 10.1038/s41586-018-0631-z.
- (13) Shirane, G.; Minkiewicz, V. J.; Nathans, R. Spin Waves in 3d Metals. *Journal of Applied Physics* **1968**, *39* (2), 383-390. DOI: 10.1063/1.2163453.
- (14) Birgeneau, R. J.; Guggenheim, H. J.; Shirane, G. Neutron Scattering Investigation of Phase Transitions and Magnetic Correlations in the Two-Dimensional Antiferromagnets K₂NiF₄, Rb₂MnF₄, Rb₂FeF₄. *Phys Rev B* **1970**, *1* (5), 2211-2230. DOI: 10.1103/PhysRevB.1.2211.
- (15) Samuelsen, E. J.; Shirane, G. Inelastic neutron scattering investigation of spin waves and magnetic interactions in α -Fe₂O₃. *physica status solidi (b)* **1970**, *42* (1), 241-256. DOI: 10.1002/pssb.19700420125.

- (16) Hutchings, M. T.; Samuelsen, E. J. Measurement of Spin-Wave Dispersion in NiO by Inelastic Neutron Scattering and Its Relation to Magnetic Properties. *Phys Rev B* **1972**, *6* (9), 3447-3461. DOI: 10.1103/PhysRevB.6.3447.
- (17) Boothroyd, A. T. *Principles of Neutron Scattering from Condensed Matter*; 2020. DOI: 10.1093/oso/9780198862314.001.0001.
- (18) Balkanski, M.; Jouanne, M.; Scagliotti, M. Magnetic ordering induced Raman scattering in FePS₃ and NiPS₃ layered compounds. *Pure and Applied Chemistry* **1987**, *59* (10), 1247-1252. DOI: 10.1351/pac198759101247.
- (19) Kim, K.; Lim, S. Y.; Lee, J. U.; Lee, S.; Kim, T. Y.; Park, K.; Jeon, G. S.; Park, C. H.; Park, J. G.; Cheong, H. Suppression of magnetic ordering in XXZ-type antiferromagnetic monolayer NiPS₃. *Nat Commun* **2019**, *10*, 345. DOI: 10.1038/s41467-018-08284-6.
- (20) Kang, S.; Kim, K.; Kim, B. H.; Kim, J.; Sim, K. I.; Lee, J. U.; Lee, S.; Park, K.; Yun, S.; Kim, T.; et al. Coherent many-body exciton in van der Waals antiferromagnet NiPS₃. *Nature* **2020**, *583* (7818), 785-789. DOI: 10.1038/s41586-020-2520-5.
- (21) Wang, X. Z.; Cao, J.; Lu, Z. G.; Cohen, A.; Kitadai, H.; Li, T. S.; Tan, Q. S.; Wilson, M.; Lui, C. H.; Smirnov, D.; et al. Spin-induced linear polarization of photoluminescence in antiferromagnetic van der Waals crystals. *Nat Mater* **2021**, *20* (7), 964-970. DOI: 10.1038/s41563-021-00968-7.
- (22) Kim, D. S.; Huang, D.; Guo, C.; Li, K.; Rocca, D.; Gao, F. Y.; Choe, J.; Lujan, D.; Wu, T. H.; Lin, K. H.; et al. Anisotropic Excitons Reveal Local Spin Chain Directions in a van der Waals Antiferromagnet. *Advanced Materials* **2023**, *35* (19), 2206585. DOI: 10.1002/adma.202206585.

- (23) Wildes, A. R.; Stewart, J. R.; Le, M. D.; Ewings, R. A.; Rule, K. C.; Deng, G.; Anand, K. Magnetic dynamics of NiPS₃. *Phys Rev B* **2022**, *106* (17). DOI: 10.1103/PhysRevB.106.174422.
- (24) Scheie, A.; Park, P.; Villanova, J. W.; Granroth, G. E.; Sarkis, C. L.; Zhang, H.; Stone, M. B.; Park, J.-G.; Okamoto, S.; Berlijn, T.; et al. Spin wave Hamiltonian and anomalous scattering in NiPS₃. *Phys Rev B* **2023**, *108*, 104402. DOI: 10.1103/PhysRevB.108.104402.
- (25) Belvin, C. A.; Baldini, E.; Ozel, I. O.; Mao, D.; Po, H. C.; Allington, C. J.; Son, S.; Kim, B. H.; Kim, J.; Hwang, I.; et al. Exciton-driven antiferromagnetic metal in a correlated van der Waals insulator. *Nat Commun* **2021**, *12* (1), 4837. DOI: 10.1038/s41467-021-25164-8.
- (26) Afanasiev, D.; Hortensius, J. R.; Matthiesen, M.; Manas-Valero, S.; Siskins, M.; Lee, M.; Lesne, E.; van Der Zant, H. S. J.; Steeneken, P. G.; Ivanov, B. A.; et al. Controlling the anisotropy of a van der Waals antiferromagnet with light. *Sci Adv* **2021**, *7* (23), eabf3096. DOI: 10.1126/sciadv.abf3096.
- (27) Mehlawat, K.; Alfonsov, A.; Selter, S.; Shemerliuk, Y.; Aswartham, S.; Buchner, B.; Kataev, V. Low-energy excitations and magnetic anisotropy of the layered van der Waals antiferromagnet Ni₂P₂S₆. *Phys Rev B* **2022**, *105* (21), 214427. DOI: 10.1103/PhysRevB.105.214427.
- (28) Fleury, P. A.; Loudon, R. Scattering of Light by One- and Two-Magnon Excitations. *Physical Review* **1968**, *166* (2), 514-530. DOI: 10.1103/PhysRev.166.514.
- (29) Wildes, A. R.; Simonet, V.; Ressouche, E.; McIntyre, G. J.; Avdeev, M.; Suard, E.; Kimber, S. A. J.; Lancon, D.; Pepe, G.; Moubaraki, B.; et al. Magnetic structure of the quasi-two-dimensional antiferromagnet NiPS₃. *Phys Rev B* **2015**, *92* (22), 224408. DOI: 10.1103/PhysRevB.92.224408.

- (30) Kim, S. Y.; Kim, T. Y.; Sandilands, L. J.; Sinn, S.; Lee, M. C.; Son, J.; Lee, S.; Choi, K. Y.; Kim, W.; Park, B. G.; et al. Charge-Spin Correlation in van der Waals Antiferromagnet NiPS₃. *Phys Rev Lett* **2018**, *120* (13), 136402. DOI: 10.1103/PhysRevLett.120.136402.
- (31) Bramwell, S. T.; Holdsworth, P. C. W. Magnetization - a Characteristic of the Kosterlitz-Thouless-Berezinskii Transition. *Phys Rev B* **1994**, *49* (13), 8811-8814. DOI: 10.1103/PhysRevB.49.8811.
- (32) Campostrini, M.; Hasenbusch, M.; Pelissetto, A.; Rossi, P.; Vicari, E. Critical exponents and equation of state of the three-dimensional Heisenberg universality class. *Phys Rev B* **2002**, *65* (14), 144520. DOI: 10.1103/PhysRevB.65.144520.
- (33) Jana, D.; Kapuscinski, P.; Mohelsky, I.; Vaclavkova, D.; Breslavetz, I.; Orlita, M.; Faugeras, C.; Potemski, M. Magnon gap excitations and spin-entangled optical transition in the van der Waals antiferromagnet NiPS₃. *Phys Rev B* **2023**, *108* (11). DOI: 10.1103/PhysRevB.108.115149.
- (34) Zeliang Sun, G. Y., Mengqi Huang, Chengkang Zhou, Nan Huang, Qiuyang Li, Zhipeng Ye, Cyn-thia Nnokwe, Hui Deng, David Mandrus, Zi Yang Meng, Kai Sun, Chunhui Du, Rui He, Liuyan Zhao. Dimensionality crossover to 2D vestigial nematicity from 3D zigzag antiferromagnetism in an XY-type honeycomb van der Waals magnet. *ArXiv* **2023**, 2311.03493. DOI: 10.48550/arXiv.2311.03493.
- (35) Shastry, B. S.; Shraiman, B. I. Theory of Raman-Scattering in Mott-Hubbard Systems. *Phys Rev Lett* **1990**, *65* (8), 1068-1071. DOI: DOI 10.1103/PhysRevLett.65.1068.
- (36) Koshibae, W.; Ohta, Y.; Maekawa, S. Theory of Dzyaloshinski-Moriya Antiferromagnetism in Distorted CuO₂ and NiO₂ Planes. *Phys Rev B* **1994**, *50* (6), 3767-3778. DOI: 10.1103/PhysRevB.50.3767.

- (37) Joy, P. A.; Vasudevan, S. Magnetism in the Layered Transition-Metal Thiophosphates MPS3 (M = Mn, Fe, and Ni). *Phys Rev B* **1992**, *46* (9), 5425-5433. DOI: DOI 10.1103/PhysRevB.46.5425.
- (38) Banda, E. J. K. B. Optical absorption of NiPS3 in the near-infrared, visible and near-ultraviolet regions. *Journal of Physics C: Solid State Physics* **1986**, *19* (36), 7329-7335. DOI: 10.1088/0022-3719/19/36/023.
- (39) Afanasiev, D.; Hortensius, J. R.; Matthiesen, M.; Mañas-Valero, S.; Šiškins, M.; Lee, M.; Lesne, E.; van der Zant, H. S. J.; Steeneken, P. G.; Ivanov, B. A.; et al. Controlling the anisotropy of a van der Waals antiferromagnet with light. *Sci Adv* **2021**, *7* (23). DOI: 10.1126/sciadv.abf3096.
- (40) Wang, X.; Cao, J.; Li, H.; Lu, Z.; Cohen, A.; Haldar, A.; Kitadai, H.; Tan, Q.; Burch, K. S.; Smirnov, D.; et al. Electronic Raman scattering in the 2D antiferromagnet NiPS₃. *Sci Adv* **2022**, *8* (2). DOI: 10.1126/sciadv.abl7707.
- (41) Tan, Q.; Luo, W.; Li, T.; Cao, J.; Kitadai, H.; Wang, X.; Ling, X. Charge-transfer-enhanced d–d emission in antiferromagnetic NiPS₃. *Applied Physics Reviews* **2022**, *9* (4). DOI: 10.1063/5.0107065.
- (42) McCreary, A.; Simpson, J. R.; Mai, T. T.; McMichael, R. D.; Douglas, J. E.; Butch, N.; Dennis, C.; Aguilar, R. V.; Walker, A. R. H. Quasi-two-dimensional magnon identification in antiferromagnetic FePS₃ via magneto-Raman spectroscopy. *Phys Rev B* **2020**, *101* (6), 064416. DOI: 10.1103/PhysRevB.101.064416.
- (43) Kuo, C. T.; Neumann, M.; Balamurugan, K.; Park, H. J.; Kang, S.; Shiu, H. W.; Kang, J. H.; Hong, B. H.; Han, M.; Noh, T. W.; et al. Exfoliation and Raman Spectroscopic Fingerprint of Few-Layer NiPS₃ Van der Waals Crystals. *Sci Rep-Uk* **2016**, *6*, 20904. DOI: 10.1038/srep20904.

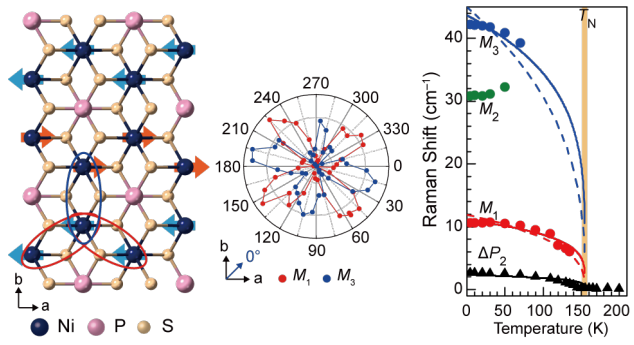
- (44) Lee, Y.; Kim, C.; Son, S.; Cui, J.; Park, G.; Zhang, K.-X.; Oh, S.; Cheong, H.; Kleibert, A.; Park, J.-G. Imaging Thermally Fluctuating Néel Vectors in van der Waals Antiferromagnet NiPS₃. *Nano Lett* **2024**, *24* (20), 6043-6050. DOI: 10.1021/acs.nanolett.4c00804.
- (45) Granroth, G. E.; Vandergriff, D. H.; Nagler, S. E. SEQUOIA: A fine resolution chopper spectrometer at the SNS. *Physica B* **2006**, *385-86*, 1104-1106. DOI: 10.1016/j.physb.2006.05.379.
- (46) Granroth, G. E.; Kolesnikov, A. I.; Sherline, T. E.; Clancy, J. P.; Ross, K. A.; Ruff, J. P. C.; Gaulin, B. D.; Nagler, S. E. SEQUOIA: A Newly Operating Chopper Spectrometer at the SNS. *J Phys Conf Ser* **2010**, *251*, 012058. DOI: 10.1088/1742-6596/251/1/012058.
- (47) Mason, T. E.; Abernathy, D.; Anderson, I.; Ankner, J.; Egami, T.; Ehlers, G.; Ekkebus, A.; Granroth, G.; Hagen, M.; Herwig, K.; et al. The Spallation Neutron Source in Oak Ridge: A powerful tool for materials research. *Physica B* **2006**, *385-86*, 955-960. DOI: 10.1016/j.physb.2006.05.281.
- (48) Ewings, R. A.; Buts, A.; Le, M. D.; van Duijn, J.; Bustinduy, I.; Perring, T. G. HORACE: Software for the analysis of data from single crystal spectroscopy experiments at time-of-flight neutron instruments. *Nucl Instrum Meth A* **2016**, *834*, 132-142. DOI: 10.1016/j.nima.2016.07.036.
- (49) Toth, S.; Lake, B. Linear spin wave theory for single-Q incommensurate magnetic structures. *J Phys-Condens Mat* **2015**, *27* (16), 166002. DOI: 10.1088/0953-8984/27/16/166002.
- (50) Zhang, H.; Batista, C. D. Classical spin dynamics based on SU(N) coherent states. *Phys Rev B* **2021**, *104* (10), 104409. DOI: 10.1103/PhysRevB.104.104409.

(51) Dahlbom, D.; Zhang, H.; Miles, C.; Bai, X. J.; Batista, C. D.; Barros, K. Geometric integration of classical spin dynamics via a mean-field Schrodinger equation. *Phys Rev B* **2022**, *106* (5), 054423. DOI: 10.1103/PhysRevB.106.054423.

(52) Dahlbom, D.; Miles, C.; Zhang, H.; Batista, C. D.; Barros, K. Langevin dynamics of generalized spins as SU(N) coherent states. *Phys Rev B* **2022**, *106* (23), 235154. DOI: 10.1103/PhysRevB.106.235154.

(53) T. Inui, Y. T., Y. Onodera. *Group Theory and Its Applications in Physics*; Springer-Verlag, 1990.

For Table of Contents Only



Supporting Information

Direct Observation and Analysis of Low-Energy Magnons with Raman Spectroscopy in Atomically Thin NiPS₃

Woongki Na,^{† #} Pyeongjae Park,^{‡,§,#} Siwon Oh,^{†,#} Junghyun Kim,[‡] Allen Scheie,[⊥] David Alan Tennant,[¶] Hyun Cheol Lee,^{†,*} Je-Geun Park^{‡,*} Hyeonsik Cheong,^{†,*}

[†]Department of Physics, Sogang University, Seoul 04107, Korea

[‡]Department of Physics and Astronomy, Seoul National University, Seoul 08826, Korea

[§]Materials Science and Technology Division, Oak Ridge National Laboratory, Oak Ridge, Tennessee 37831, USA

[⊥]MPA-Q, Los Alamos National Laboratory, Los Alamos, NM 87545, USA

[¶]Department of Physics and Astronomy, University of Tennessee, Knoxville, TN 37996, USA and
Department of Materials Science and Engineering, University of Tennessee, Knoxville, TN 37996,
USA

Contents:

- **Note S1.** Calculation of Polarization Dependence
- **Figure S1.** Determination of crystal axes.
- **Figure S2.** Low-frequency Raman spectra at 50 K measured by using lasers with different wavelengths.
- **Figure S3.** Temperature dependence of polarized Raman spectra for 6L, 5L, and 4L NiPS₃.
- **Figure S4.** Temperature dependence of polarized Raman spectra for 3L, 2L, and 1L NiPS₃.
- **Figure S5.** Temperature dependence of M₁ magnon peak and ΔP₂ for few-layer NiPS₃.
- **Figure S6.** INS data of NiPS₃ along the momentum contour [H, 1/2, 1] (r.l.u.).
- **Figure S7.** INS cross-sections of NiPS₃ at Q = [0, 1, 0] and [0, 1, 1] calculated from linear spin-wave theory and Equation 4 of the main text.

Note S1. Calculation of Polarization Dependence

1) Parametrization of lattice sites

The two-dimensional crystal structure¹ of NiPS₃ can be parameterized as follows. The Ni ions form a honeycomb lattice, which can be described as a triangular lattice with a basis. Let a be the distance between Ni ions, then the triangular lattice can be spanned by

$$\vec{a}_1 = \sqrt{3}a\hat{\mathbf{a}}, \quad \vec{a}_2 = \frac{\sqrt{3}}{2}a\hat{\mathbf{a}} + \frac{3}{2}a\hat{\mathbf{b}}, \quad (\text{S1})$$

$\hat{\mathbf{a}}$ is the unit vector along \mathbf{a} -axis, etc. The honeycomb lattice can be described with a basis at $\eta = a\hat{\mathbf{b}}$.

Honeycomb lattice: $\mathbf{R}_{m_1, m_2} = m_1\vec{a}_1 + m_2\vec{a}_2, \quad \mathbf{R}_{m_1, m_2} + \eta$.

Second, put a Ni ion at the center of a hexagon formed by 6 surrounding S ions. This implies that the trigonal axis of the undeformed octahedron is along the c -axis. The distance in the ab -plane between Ni ion and S ion is $a/\sqrt{3} = a'$. The planar positions of the six S ions relative to the center, which is taken to be the origin, can be written as follows:

$$\begin{aligned} \delta_{1+} &= a'\hat{\mathbf{a}}, & \delta_{2-} &= \frac{a'}{2}\hat{\mathbf{a}} + \frac{\sqrt{3}}{2}a'\hat{\mathbf{b}}, \\ \delta_{3+} &= -\frac{a'}{2}\hat{\mathbf{a}} + \frac{\sqrt{3}}{2}a'\hat{\mathbf{b}}, & \delta_{4-} &= -a'\hat{\mathbf{a}}, \\ \delta_{5+} &= -\frac{a'}{2}\hat{\mathbf{a}} - \frac{\sqrt{3}}{2}a'\hat{\mathbf{b}}, & \delta_{6-} &= +\frac{a'}{2}\hat{\mathbf{a}} - \frac{\sqrt{3}}{2}a'\hat{\mathbf{b}}, \end{aligned} \quad (\text{S2})$$

where \pm subscripts indicate whether the S-ion is above or below the Ni plane.

We note that this crystal structure is edge-sharing, and so each S ion can be connected to two Ni ions by nearest-neighbor hopping. Now, the S-ion sites can be parametrized by

$$\mathbf{R}_{m_1, m_2, (0, \eta)} + \delta_{i\pm}. \quad (\text{S3})$$

2) Tight-binding model Hamiltonian

We transcribe the Hamiltonian by Koshibae *et al.*², which is being adapted to the crystal structure of

NiPS₃. The lattice sites have been fully parameterized in Section 1.1, and they will be denoted compactly in this section to avoid cumbersome notations. Let \mathbf{R} and \mathbf{R}_p denote a generic position of Ni and S ions, respectively. The tight-binding Hamiltonian consists of the on-site and hopping terms (the electron-photon interaction Hamiltonian will be treated in the next section).

$$\hat{H}_{\text{t-b}} = \hat{H}_{\text{on-site}} + \hat{H}_{\text{hop}} \quad (\text{S4})$$

Below $d_{\mathbf{R}\alpha\sigma}^\dagger$ and $p_{\mathbf{R}_p a\sigma}^\dagger$ are the *hole creation operators* with spin σ for Ni ion and S ion at site \mathbf{R} , \mathbf{R}_p , respectively. $\alpha = 0, 1$ is the e_g orbital index, and $a = p_x, p_y, p_z$ is the p-orbital index. The number operators are defined as

$$n_{\mathbf{R}\alpha\sigma}^d = d_{\mathbf{R}\alpha\sigma}^\dagger d_{\mathbf{R}\alpha\sigma}, \quad n_{\mathbf{R}_p a\sigma}^p = p_{\mathbf{R}_p a\sigma}^\dagger p_{\mathbf{R}_p a\sigma}. \quad (\text{S5})$$

The spin summed number operator is denoted by $n_{\mathbf{R}\alpha}^d$, etc. The on-site Hamiltonian consists of the site-energy term, Coulomb repulsion term, and spin-orbit interaction term.

$$\begin{aligned} \hat{H}_{\text{on-site}} &= \sum_{\mathbf{R}, \alpha, \sigma} \epsilon_\alpha n_{\mathbf{R}\alpha\sigma}^d + \sum_{\mathbf{R}_p, a, \sigma} \epsilon_a n_{\mathbf{R}_p a\sigma}^p && \text{site energy} \\ &+ U \sum_{\mathbf{R}, \alpha} n_{\mathbf{R}\alpha\uparrow}^d n_{\mathbf{R}\alpha\downarrow}^d && \text{Hubbard Coulomb repulsion} \\ &+ U_{01} \sum_{\mathbf{R}} n_{\mathbf{R}0}^d n_{\mathbf{R}1}^d && \text{inter-orbital Coulomb repulsion} \\ &+ \lambda \sum_{\mathbf{R}} (\mathbf{L}_{\mathbf{R}}^{\text{I}} \cdot \mathbf{S}_{\mathbf{R}}^{\text{I}} + \mathbf{L}_{\mathbf{R}}^{\text{II}} \cdot \mathbf{S}_{\mathbf{R}}^{\text{II}}) && \text{spin-orbit interaction,} \end{aligned} \quad (\text{S6})$$

where I and II denote two holes on a Ni ion, and other notations are self-explanatory. $\epsilon_0 \approx \epsilon_1$ is assumed for d-orbitals, while the p -orbital site energies can be split by trigonal distortion. All parameters of the Hamiltonian should be regarded as phenomenological. The explicit form of the operators of spin-orbit interaction is given by

$$\mathbf{L}_{\mathbf{R}} \cdot \mathbf{S}_{\mathbf{R}} = \sum_{i=x,y,z} (L^i)_{\alpha\alpha'} \left(\frac{\sigma^i}{2}\right)_{\sigma\sigma'} d_{\mathbf{R}\alpha\sigma}^\dagger d_{\mathbf{R}\alpha'\sigma'}. \quad (\text{S7})$$

$(L^i)_{\alpha\alpha'}$ is the matrix element of orbital angular momentum $l = 2$ operator, and σ^i is the i -th Pauli sigma matrix.

The spin-orbit coupling is treated perturbatively. In the first order, it can modify the hopping

amplitude to become spin-dependent. This contribution will induce a spin-dependent electron-photon coupling, which we ignore for simplicity (analytical computations turn out to be too formidable). In the second order, it gives rise to the *single ion anisotropy*, which is responsible for the planar spin configuration³, while it does not couple to photon because it is an on-site interaction.

The hopping Hamiltonian between Ni and S ion is given by

$$\hat{H}_{\text{hop}} = \sum_{\langle \mathbf{R}, \mathbf{R}_p \rangle a, \alpha, \sigma} (t_{\mathbf{R}, \mathbf{R}_p}^{\alpha\alpha} d_{\mathbf{R}\alpha\sigma}^\dagger p_{\mathbf{R}_p, a, \sigma} + \text{h.c.}), \quad (\text{S8})$$

where $t_{\mathbf{R}, \mathbf{R}_p}^{\alpha\alpha}$ is the nearest neighbor hopping amplitude and h.c. stands for the Hermitian conjugate.

3) Electron-photon interaction Hamiltonian

In visible range, the position dependence of the vector potential can often be neglected so that the line integral in the exponent of the Peierls phase can be simplified to

$$\exp\left(-i \frac{e}{\hbar c} (\mathbf{R}_i - \mathbf{R}_j) \cdot \mathbf{A}(t)\right) \quad (\text{S9})$$

Then the Peierls coupling to the hopping Hamiltonian Equation S8 takes the following form:

$$\hat{H}_{\text{hop+em}} = \sum_{\langle \mathbf{R}, \mathbf{R}_p \rangle a, \alpha, \sigma} (t_{\mathbf{R}, \mathbf{R}_p}^{\alpha\alpha} \exp\left[-i \frac{e}{\hbar c} \mathbf{A}(t) \cdot (\mathbf{R} - \mathbf{R}_p)\right] d_{\mathbf{R}\alpha\sigma}^\dagger p_{\mathbf{R}_p, a, \sigma} + \text{h.c.}). \quad (\text{S10})$$

The expansion of $H_{\text{hop+em}}$ with respect to the vector potential $\mathbf{A}(t)$ in the first order gives the electron-photon interaction Hamiltonian for the magnetic Raman scattering.

$$\hat{H}_{\text{e-photon}} = -\frac{e}{c} \mathbf{A}(t) \cdot \mathbf{j}, \quad (\text{S11})$$

where the current operator is

$$\mathbf{j} = \frac{i}{\hbar} \sum_{\langle \mathbf{R}, \mathbf{R}_p \rangle a, \alpha, \sigma} (\mathbf{R} - \mathbf{R}_p) t_{\mathbf{R}, \mathbf{R}_p}^{\alpha\alpha} (d_{\mathbf{R}\alpha\sigma}^\dagger p_{\mathbf{R}_p, a, \sigma} - \text{h.c.}). \quad (\text{S12})$$

The direct coupling between the photon polarization and the crystal structure manifests in Equation S11. This implies that the deformation of the crystal structure is directly reflected in the polarization dependence. We again emphasize that the spin-orbit interaction is not considered in our theoretical

calculation of the effective scattering Hamiltonian.

4) Some details of perturbation calculations

A key identity in the derivation of the effective scattering Hamiltonian is

$$\sum_{\sigma, \sigma'} d_{\mathbf{R}\alpha\sigma}^\dagger d_{\mathbf{R}'\alpha'\sigma'} d_{\mathbf{R}'\alpha'\sigma}^\dagger d_{\mathbf{R}\alpha\sigma} = (-2) \mathbf{S}_{\mathbf{R}\alpha} \cdot \mathbf{S}_{\mathbf{R}'\alpha'} + \text{constant}, \quad (\text{S13})$$

which is valid in the low-energy Hilbert space. By taking the symmetric combination of the above operator and using the Wigner-Eckart theorem² we can obtain the effective Hamiltonian in terms of spin-1 operator.

Let us consider a scattering process in which a photon is absorbed first. In this case, some of the explicit expressions of resolvents Equation 7 of the main text are as follows ($\epsilon_d = \epsilon_{0,1}$, and $\hbar\omega_i$ is the energy of the incident photon).

$$G = \frac{1}{\epsilon_d + U_{01} + \hbar\omega_i - \epsilon_{p_a}}, \quad \text{one S-ion hole with orbital } p_a \text{ being occupied.} \quad (\text{S14})$$

$$G = \frac{1}{\hbar\omega_i - U}, \quad \text{one orbital of Ni ion being doubly occupied.} \quad (\text{S15})$$

$$G = \frac{1}{2\epsilon_d + 2U_{01} + \hbar\omega_i - \epsilon_{p_a} - \epsilon_{p_b}}. \quad \text{Two S ion holes in orbitals } p_a, p_b \text{ being doubly occupied} \quad (\text{S16})$$

The case where the photon emission occurs first can be handled similarly. Using the above results, we can compute the amplitudes $\mathcal{M}_{\text{Ni/S}}$ of Equation 9 of the main text.

One example of the exchange amplitude via doubly occupied Ni ion with the following exchange path $\mathbf{R} \rightarrow \mathbf{R} + \boldsymbol{\delta}_1 \rightarrow \mathbf{R}' \rightarrow \mathbf{R} + \boldsymbol{\delta}_1 \rightarrow \mathbf{R}$ is given by

$$\sum_{a,b} \frac{1}{\epsilon_d + U_{01} + \hbar\omega_i - \epsilon_{p_a}} \frac{1}{\hbar\omega_i - U} \frac{1}{\epsilon_d + U_{01} + \hbar\omega_i - \epsilon_{p_b}} t_{0a|\delta_1} t_{0a|\delta_1'} t_{0b|\delta_1'} t_{0b\delta_1} [\mathbf{A}_i \cdot \boldsymbol{\delta}_1] [\mathbf{A}_s^* \cdot (-\boldsymbol{\delta}_1)], \quad (\text{S17})$$

where $\mathbf{A}_{i,s}$ is the vector potential of the incoming and the scattered photon, respectively.

Next, let us consider the exchange amplitude via doubly occupied S ion with the following

exchange path

$$\mathbf{R} \rightarrow \mathbf{R} + \delta_1 \rightarrow \mathbf{R} \quad \text{and} \quad \mathbf{R}' \rightarrow \mathbf{R}' + \delta_1' \rightarrow \mathbf{R}' \quad (\text{S18})$$

In the above path, the S-ion 1 is doubly occupied, and the photon is absorbed and emitted in the hop

$\mathbf{R} \leftrightarrow \mathbf{R} + \delta_1$. The associated amplitude is given by

$$\sum_{a,b} \frac{1}{\epsilon_d + U_{01} + \hbar\omega_i - \epsilon_{p_a}} \frac{1}{2\epsilon_d + 2U_{01} + \hbar\omega_i - \epsilon_{p_a} - \epsilon_{p_b}} \left(\frac{1}{\epsilon_d + U_{01} + \hbar\omega_i - \epsilon_{p_a}} + \frac{1}{\epsilon_d + U_{01} + \hbar\omega_i - \epsilon_{p_b}} \right) \quad (\text{S19})$$

$$\times t_{0a}^2 t_{0b}^2 [\mathbf{A}_i \cdot \delta_1] [\mathbf{A}_s^* \cdot (-\delta_1)]$$

There are many other possible exchange paths, and the corresponding amplitudes can be computed in an entirely identical way.

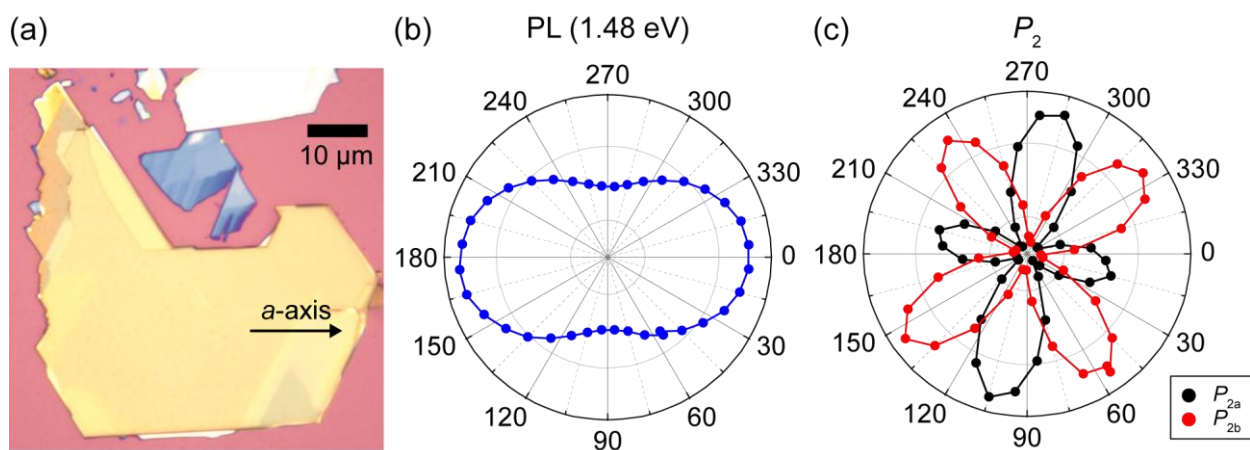


Figure S1. Determination of crystal axes. a) Optical microscope image of sample. b,c) Polarization dependence of the PL at 1.48 eV and the split P_2 peaks at 3.5 K.

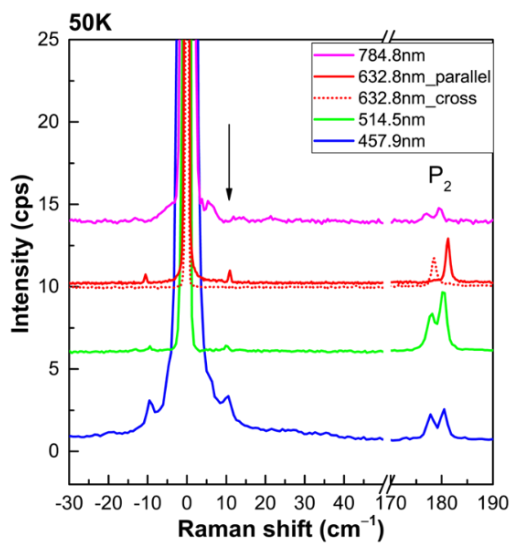


Figure S2. Low-frequency Raman spectra at 50 K measured by using lasers with different wavelengths.

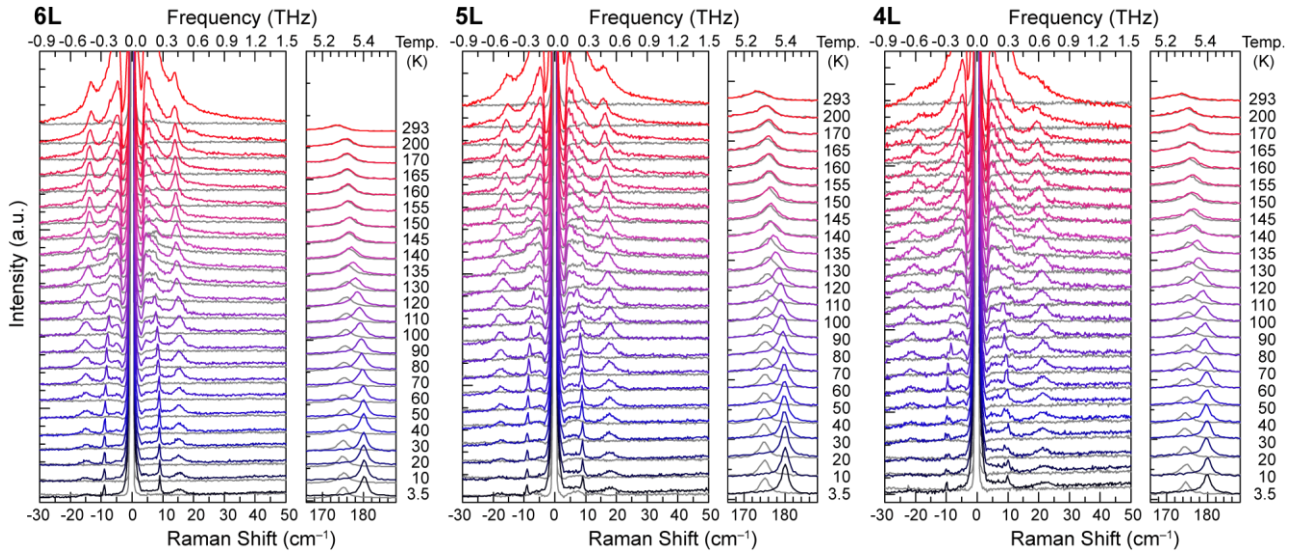


Figure S3. Temperature dependence of polarized Raman spectra for 6L, 5L, and 4L NiPS₃. The colored spectra are measured in the $z(xx)\bar{z}$ polarization configuration and the grey spectra in $z(xy)\bar{z}$.

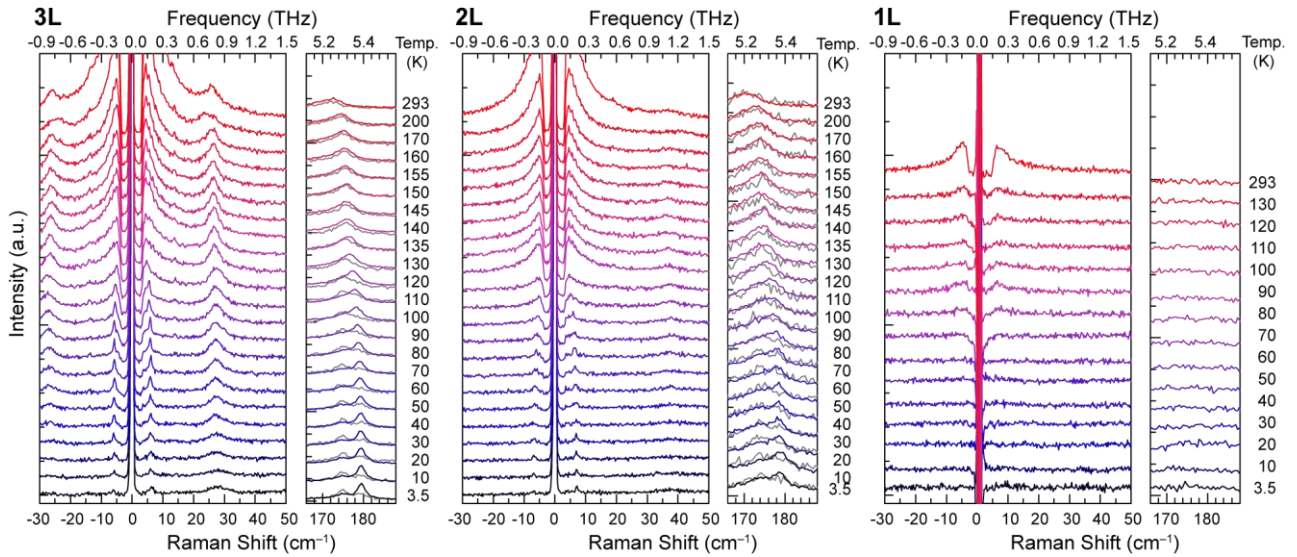


Figure S4. Temperature dependence of polarized Raman spectra for 3L, 2L, and 1L NiPS₃ measured in the $z(xx)\bar{z}$ polarization configuration.

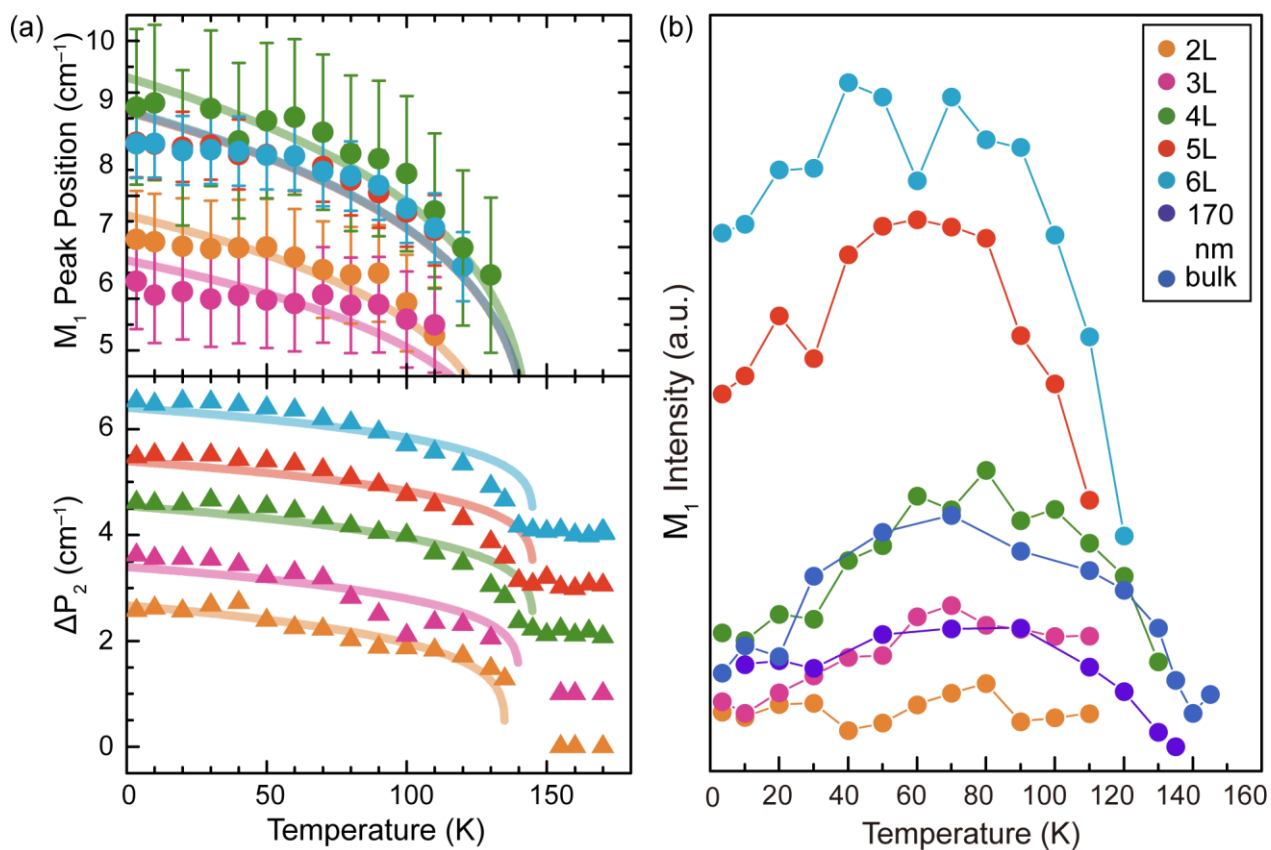


Figure S5. a) Temperature dependence of M₁ magnon peak position and ΔP₂ for few-layer NiPS₃. The data for ΔP₂ are offset vertically for clarity. The curves show temperature dependence of $[1 - T/T_N]^\beta$ with the exponent of 0.23. b) Temperature dependence of M₁ magnon peak intensity.

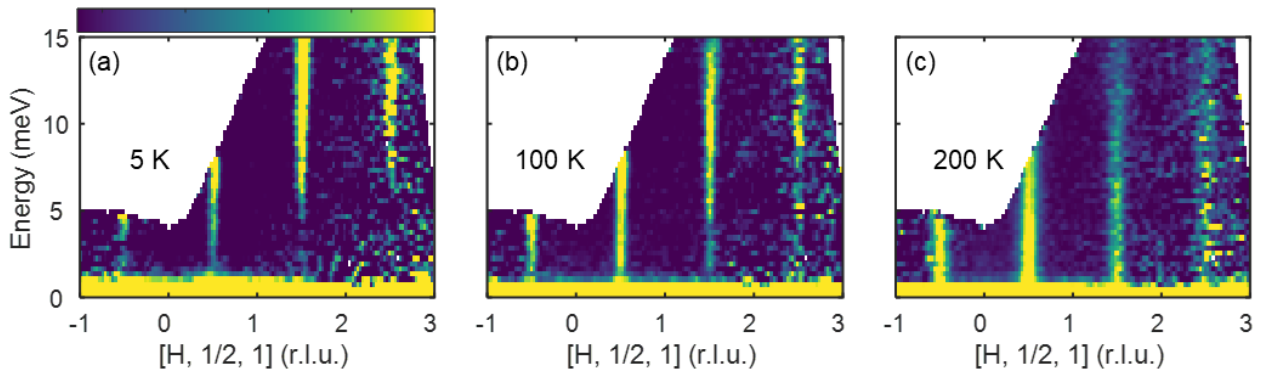


Figure S6. INS data of NiPS₃ along the momentum contour $[H, 1/2, 1]$ (r.l.u.). Magnon dispersion down to ~ 1.5 meV is clearly visible at $[1/2, 1/2, 1]$.

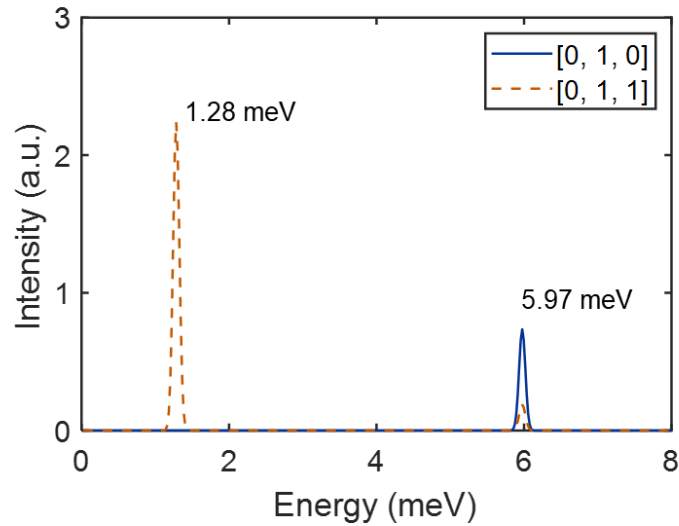


Figure S7. INS cross-sections of NiPS₃ at $Q = [0, 1, 0]$ (solid blue curve) and $[0, 1, 1]$ (dashed orange curve) calculated from linear spin-wave theory and Equation 4 of the main text. For a clear demonstration of magnon eigenvalues, the cross-sections were convoluted by a Gaussian function with the full-width-at-half-maximum of 0.1 meV. Note that the calculation results shown in Figure 5c-f are different from those shown in this figure as they include the effects of the momentum resolution and the experimental bin width.

References

- (1) Kang, S.; Kim, K.; Kim, B. H.; Kim, J.; Sim, K. I.; Lee, J. U.; Lee, S.; Park, K.; Yun, S.; Kim, T.; et al. Coherent many-body exciton in van der Waals antiferromagnet NiPS₃. *Nature* **2020**, *583* (7818), 785-789. DOI: 10.1038/s41586-020-2520-5.
- (2) Koshibae, W.; Ohta, Y.; Maekawa, S. Theory of Dzyaloshinski-Moriya Antiferromagnetism in Distorted CuO₂ and NiO₂ Planes. *Phys Rev B* **1994**, *50* (6), 3767-3778. DOI: 10.1103/PhysRevB.50.3767.
- (3) Afanasiev, D.; Hortensius, J. R.; Matthiesen, M.; Manas-Valero, S.; Siskins, M.; Lee, M.; Lesne, E.; van Der Zant, H. S. J.; Steeneken, P. G.; Ivanov, B. A.; et al. Controlling the anisotropy of a van der Waals antiferromagnet with light. *Sci Adv* **2021**, *7* (23), eabf3096. DOI: 10.1126/sciadv.abf3096.